Development of A Spin Rotator for Detecting All Three Magnetization Vector Components by Spin-Polarized Scanning Electron Microscopy and Its Application for Recording Media

by

Teruo Kohashi

1997

(1)

Development of A Spin Rotator for Detecting All Three Magnetization Vector Components by Spin-Polarized Scanning Electron Microscopy and Its Application for Recording Media

by

Teruo Kohashi

1997

List of Abbreviations

SEM	scanning electron microscopy
S/N	signal to noise
C/N	carrier to noise
VTR	video tape recorder
AT_{0P}	ampere turn zero to peak

Abstract

A spin rotator has been developed for observing by spin-polarized scanning electron microscopy (spin SEM) magnetic domains with all three magnetization components of a sample surface. The spin rotator is placed between the sample and the spin detector in a spin SEM, and can rotate the polarization vector of secondary electrons by $\pi/2$. Although the spin detector itself can detect only two independent polarization components, the rotation of polarization makes third-component detection possible. The conventional spin rotator, which is a well-known energy filter named a Wien Filter, has been much improved by enlarging the focusing area by using hyperbolic cylindrical pole pieces as a magnet and several auxiliary electrodes. As a result, all the secondary electrons emitted from the area of a surface as large as 1 mm in diameter can pass the spin rotator with uniform spin rotation, and the distribution of all three magnetization components can be imaged successfully by spin SEM.

By using the spin SEM in which the spin rotator is installed, we observed recorded marks of the magneto-optical recording medium TbFeCo film. First we studied the laser power dependency of the shapes and sizes of the recorded marks on the TbFeCo film prepared on a land/groove substrate. When a higher power was used, the land/groove border acted as a barrier to the propagation of the magnetization reversal, which confirms the advantage of using a land/groove substrate for high-density recording. Besides that we looked at the underlayer roughness dependency of the recorded marks. We found that the

magnetization reversal processes depend on the underlayer roughness, which is related to the irregularity of the mark shapes and the recording noise.

Then we observed magnetic domains in the remanent magnetization state of obliquely evaporated recording media, Co-CoO films, by spin SEM. Inverse domains densely distributed in the media were found to have a closure-domain-like structure at the surface to reduce the magneto-static energy. The size of the inverse domains depends on the direction of the external magnetic fields that were applied when the remanent states were formed. Using these results, the relationship between the inverse domains and the carrier-to-noise ratio for this kind of recording media is discussed.

CONTENTS

1. Introduction

The observation of magnetic domain structures with high spatial resolution is very important not only in such fundamental fields as the study of magnetic domain walls but also in industrial applications such as magnetic recording. Especially in the field of the magnetic recording, high resolution is now indispensable since bit length is going into the sub-micron region. It is essential to observe the recorded magnetization in detail and improve the recording characteristics in order to increase the density further.

In this respect, spin-polarized scanning electron microscope (spin SEM)[1-4] is a very useful instrument for studying magnetic domain structures in high resolution. It was developed by Koike[1] *et al.* in 1984, and uses the phenomenon where the spin-polarization vector of secondary electrons emitted from ferromagnetic material is antiparallel to the magnetization vector at the originating point of the secondary electrons on the material,[5] as shown in Fig. 1.1. Figure 1.2 shows the structure of the spin SEM. The very fine probe electron beam from the electron gun is injected into the surface of the ferromagnetic sample. Polarized secondary electrons are emitted from it, which retain the spin-polarization orientation characteristics of the local region of the sample, are sent to the spin detector and spin-analyzed.

Figures 1.3 and 1.4 show the basic principle of the spin detector, which takes advantage of Mott scattering and is therefore called a Mott detector. When the high-energy polarized electrons with up- and down-spin hit a Au atom target and are

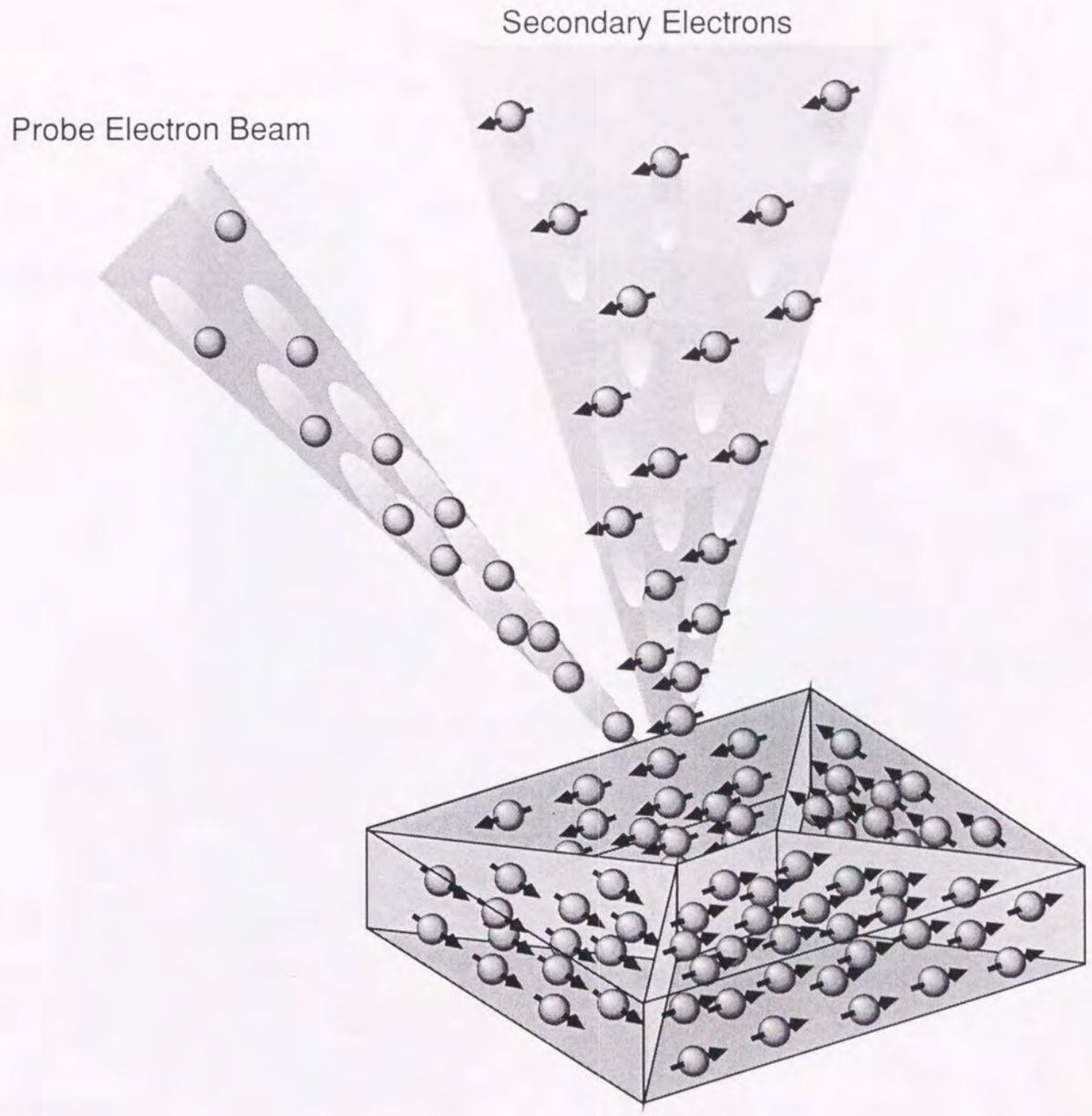

Fig. 1. 1. The spin polarization of the secondary electrons from the ferromagnetic materials.

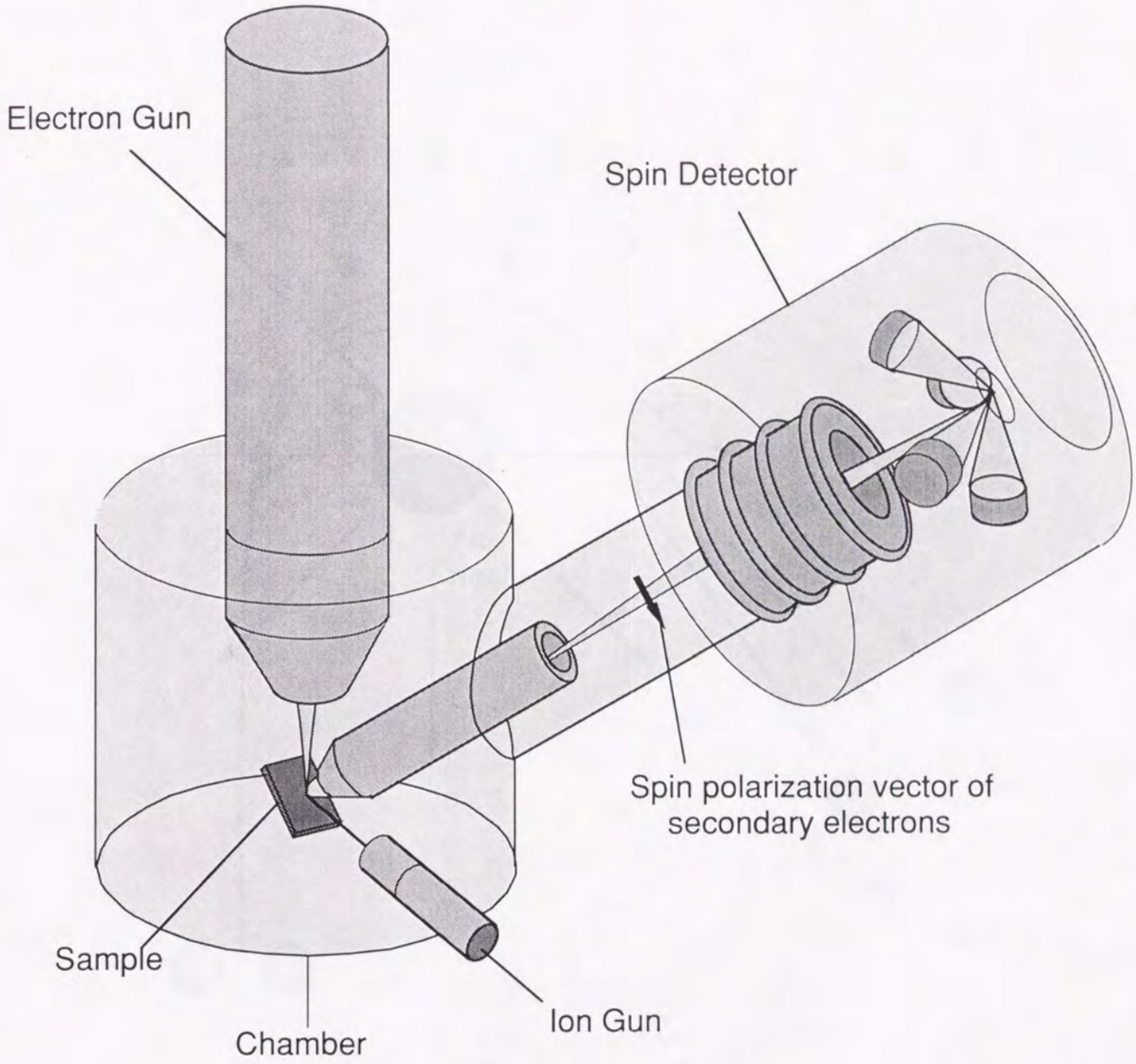

Fig. 1. 2. The structure of the spin SEM.

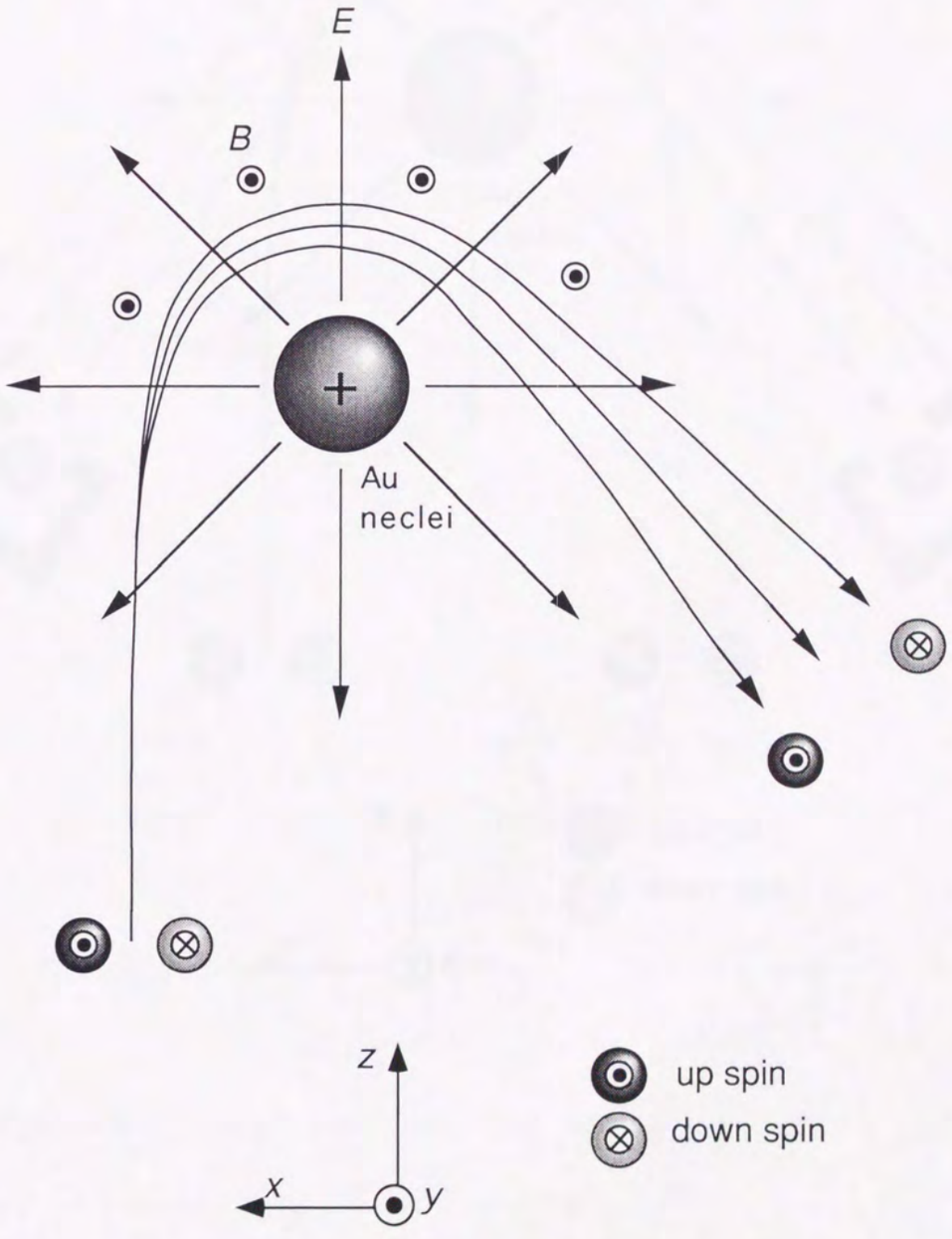

Fig. 1. 3. The motion of the electrons with up- and down-spin when they are elastically scattered at a Au atom.

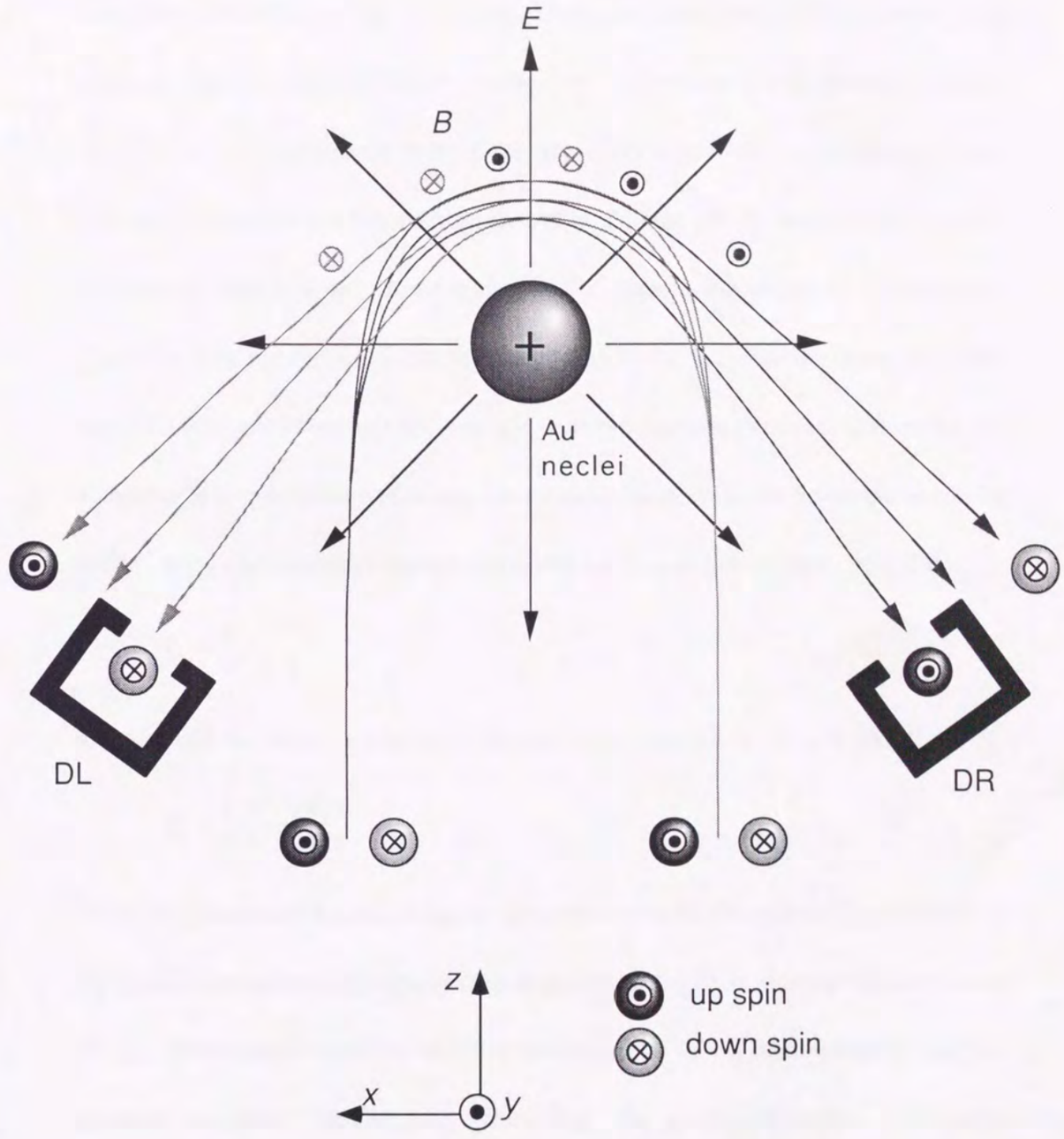

Fig. 1. 4. The motion of the electrons with up- and down-spin when they are elastically scattered at a Au atom and detected by the electron detectors, DL and DR, which are symmetrically placed to the electron trajectories.

elastically scattered as Fig. 1.3 shows, these electrons run in the magnetic field because they rotate around the Au nuclei. The interactions of the electron spin with this field, so called spin-orbit interactions, are different between the electrons with up- and down-spin. If we set two electron detectors, DL and DR, as shown in Fig. 1.4, DL detects the electrons with down-spin while DR detects the electrons with up-spin. Therefore, the number of electrons detected by these two electron detectors differ when the number of electrons with up- and down-spin among the injected electrons are different. Spin polarization P_y along the direction normal to the figure plane can be defined using the number of the electrons with up-spin and down-spin, N_+ and N_-,

$$P_y = \frac{N_+ - N_-}{N_+ + N_-}. \tag{1.1}$$

It is also defined using the number of the electrons detected by DL and DR, N_l and N_r,

$$P_y = \frac{1}{S}\frac{N_r - N_l}{N_r + N_l}. \tag{1.2}$$

Here, S is a Sherman function which is determined only by the scattering condition (in the case of the general spin polarization detector, $S \leq 0.3$). In this way we can detect the spin polarization along the direction perpendicular to the figure plane by the two electron detectors. In the Mott scattering, the spin polarization components perpendicular to the electron trajectory, P_x and P_y, can be detected setting four electron detectors, while the component parallel to the electron trajectory, P_z, cannot be detected because the spin-orbit interactions are zero.

As mentioned above, the magnetization vector can be determined at the originating point of the secondary electrons on the material and one magnetic domain

image is obtained after scanning the sample surface with the prove electron beam. This technique results in several excellent characteristics. Matsuyama *et al.* developed the spin SEM with the spatial resolution[6] of 20 nm and it has been successfully applied to in-plane recording media with the recording density in the 50-140 kFCI range.[7] Another advantage of spin SEM is that magnetization information independent of sample surface topography can be obtained. Thus, it is useful for investigating samples with uneven topographies such as a recording medium on an underlayer with surface roughness. Besides those capabilities the spin SEM can determine not only shapes of domains but also the magnetization direction and has been applied for mapping the distribution of the magnetization vector of Fe (001),[8] polycrystal[8] and amorphous[9] surfaces.

However, the spin detector used in spin SEM can detect only two polarization components perpendicular to the electron trajectory, which is based on the principle of the spin detector as mentioned before. In the case of our spin SEM configuration the magnetization perpendicular to the sample surface has not been able to be detected. Therefore our spin SEM has not been used with recording material which has mainly a perpendicular magnetization component such as magneto-optical recording media and perpendicular magnetic recording media. These magnetic recording media have recently attracted a lot of attention for achieving ultra-high density recording. Spin SEM is also expected to play an important role in this field.

The main purpose of this study is to improve our spin SEM for detecting all three magnetization components. We developed a spin rotator and set it between the sample

and the spin detector. The spin rotator rotates the spin polarization of the electrons from the undetectable direction to the detectable direction. By switching the spin rotator on and off, all the three magnetization components have become detectable in our spin SEM. Designing and building the spin rotator is explained in chapter 2.

After installing the spin rotator to the spin SEM, it was used in the studies of two kinds of recording media. In chapter 3, the observation of the recorded marks on magneto-optical recording medium TbFeCo is explained. In chapter 4 the study of the remanent magnetization on the obliquely evaporated Co-CoO film which is studied as the material for the video tapes is explained. Chapter 5 briefly summarizes the contents presented in the proceeding chapters.

references

[1]K. Koike and K.Hayakawa, Jpn. J. Appl. Phys. **23**, L187 (1984).

[2]J. Unguris, M. R. Scheinfein, D. T. Pierce, and R. J. Celotta, Appl. Phys. Lett. **55**, 2553 (1989).

[3]H. P. Oepen and J. Kirschner, Scanning Microscopy **5**, 1(1991).

[4]R. Allenspach, Physics World, March, 44(1994).

[5]J. Kirschner and K. Koike, Surf. Sci. **273**, 147(1992).

[6]H. Matsuyama, K. Koike, J. Electron Microsc. **43**, 157(1994).

[7]H. Matsuyama, K. Koike, F. Tomiyama, Y. Shiroishi, A. Ishikawa, and H. Aoi, IEEE Trans. Magn. **MAG-30**, 1327 (1994).

[8]H. Matsuyama, and K. Koike, Rev. Sci. Instrum. **62**, 970 (1991).

[9]K. Koike, H. Matsuyama, W. J. Tseng, and J. C. M. Li, Appl. Phys. Lett. **62**, 2581(1993).

2. Development of a Spin Rotator

2.1 Introduction

A spin detector used in spin SEM generally detects only two independent polarization-components normal to the trajectories of the electrons incident to the spin detector, as explained in the previous chapter. Therefore spin SEM with one spin detector have detected only two of the three magnetization components. The NIST group[1] and the Forschungszentrum group[2] have succeeded in detecting three polarization components in their spin SEMs by using two spin detectors ; one for two components, and the other for the remaining one. And it has been applied[3] for magneto-optical recording medium and analyzing all three magnetization components. It is possible, however, to detect three magnetization components with one spin detector, if we use a spin rotator. In this case the spin rotator is inserted between the sample and the spin detector. When the spin rotator is inactive, the spin detector detects two components, *e.g.* P_x and P_y, perpendicular to the trajectory. When the spin rotator is active, it rotates the polarization vector by $\pi/2$ so that the remaining parallel component P_z becomes perpendicular to the trajectory and the spin detector detects it. Since the spin rotator is simpler in structure and less expensive than the spin detector, this method keeps the whole system compact and cuts costs.

This method has already been used by Kisker *et al.*[4] to detect the parallel polarization component of electrons field-emitted from a very fine EuS tip. It is difficult, however, to apply the same kind of spin rotator as they designed to the

secondary electron beam of our spin SEM. Our estimation showed that the effective cross-sectional area of that kind of spin rotator is much smaller than the area through which the secondary electrons in the spin SEM pass. Duden and Bauer[5] developed a spin rotator to detect all three magnetization vectors by spin-polarized low energy electron microscopy (SPLEEM). In their spin rotator, however, the electron trajectories deflect by 90 degrees, which is not applicable for our spin SEM system because the electrons go straight from the sample surface to the spin detector.

In this chapter we report on a spin rotator, which has an effective cross-sectional area large enough for secondary electrons in spin SEM and makes it possible to detect all three magnetization components by one spin detector.[6]

2.2 Principle of a Spin Rotator

A Wien filter,[7] an electron optical component well known as an energy analyzer, has capability as a spin rotator. A schematic of the Wien filter is shown in Fig. 2.1. It has mutually perpendicular electric field E and magnetic field B, both perpendicular to the direction of the electron motion ($+z$-direction). These fields are adjusted so that the electro-static force cancels the Lorentz force and the electrons go straight. In this case E is expressed by

$$E = vB, \tag{2.1}$$

where v is the velocity of the electron. Equation (2.1) is the so called Wien condition.

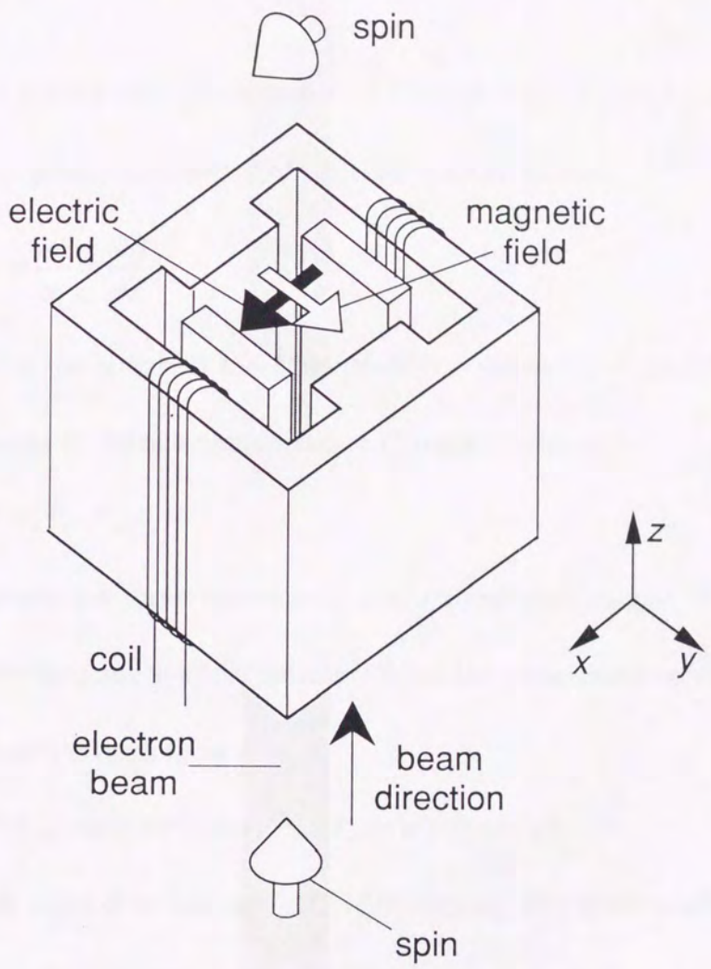

Fig. 2. 1. Principle of a spin rotator. Electrons go straight upwards in the static electric and magnetic fields because the electro-static force and Lorenz force acting on them are canceled. Their spins rotate due to the Larmor precession. [6]

The electron spin, on the other hand, rotates about the magnetic field direction due to the Larmor precession with frequency ω expressed by

$$\omega = \frac{eB}{m}, \tag{2.2}$$

where e is electronic charge and m is electron mass. Thus after passing through the filter, the polarization vector of electrons rotates by α;

$$\alpha = \frac{l\omega}{v} = \frac{leB}{mv}, \tag{2.3}$$

where l is the length of the filter. Here, we define P_x, P_y and P_z as x-, y- and z-components of the polarization vector P, respectively, *i.e.*

$$P = (P_x, P_y, P_z). \tag{2.4}$$

Among the three components, the z-component parallel to the beam direction cannot be detected in a spin detector. When the secondary electrons pass through the spin rotator, P turns to be

$$P = (P_x \cos\alpha + P_z \sin\alpha, P_y, -P_x \sin\alpha + P_z \cos\alpha). \tag{2.5}$$

When we adjust B so that $\alpha = \pi/2$ while keeping the condition of Eq. (2.1), P turns to be

$$P = (P_z, P_y, -P_x) \tag{2.6}$$

without deflection of the trajectory and P_z and P_y become detectable.

A Wien filter with uniform magnetic and electric fields has focusing effect only in the direction of the electric field, and the beam diverges in the direction of the magnetic field. Seliger[8] theoretically showed that stigmatic focus is obtained for the beam which runs in the z-direction when electric and magnetic fields are expressed by

$$\left(E_x, E_y, E_z\right) = \left(E,0,0\right), \tag{2.7}$$

$$(B_x, B_y, B_z) = (B\frac{y}{2r}, B(1+\frac{x}{2r}),0), \tag{2.8}$$

$$r = \frac{mv^2}{eE}, \tag{2.9}$$

where E_x, E_y, E_z and, B_x, B_y, B_z are the x-, y-, z-components of electric field and magnetic flux density, respectively, and r is the cyclotron radius. In these expressions the electric field is uniform and the magnetic field is a linear function of the position (here we call it type 1). The equations of the electron motion in the fields expressed by Eqs. (2.7) and (2.8) are given by

$$\ddot{x} = -\left(\frac{eB}{\sqrt{2}m}\right)^2 x \tag{2.10}$$

and

$$\ddot{y} = -\left(\frac{eB}{\sqrt{2}m}\right)^2 y\,. \tag{2.11}$$

The solutions of these equations give a simple harmonic oscillation, both in the x- and y-directions with the same frequency, and a stigmatic focusing. This is also the case in a linear electric field and a uniform magnetic field (type 2) expressed by

$$(E_x, E_y, E_z) = (E(1-\frac{x}{2r}), E\frac{y}{2r},0), \tag{2.12}$$

and

$$(B_x, B_y, B_z) = (0, B,0)\,. \tag{2.13}$$

Several Wien filters have been reported which simulate the electric and magnetic field mentioned above.[8-11]

2.3 Specification

In spin SEM we need to send all secondary electrons to the spin detector otherwise the loss of electrons increases statistical error of the measured polarization. A Wien filter has an energy analyzing capability, therefore the secondary electrons with energy spread of a few electron volts disperse spatially after passing through the filter, and some of them cannot reach the spin detector. To avoid this difficulty it is necessary to increase secondary energy so that the relative energy spread becomes small. If the energy is higher, however, the voltage necessary for the filter is higher, which might cause a vacuum discharge. Thus we need a compromise. By considering a dispersion of a typical Wien filter and the acceptance of our spin rotator, we chose the pass energy of secondary electrons in the filter to be 2 keV.

The maximum observable sample area of our spin SEM is 1 mm in diameter. We would like to keep this area even when we use a spin rotator. In this case, the cross sectional area of the spin rotator where the secondary electrons pass is 6 mm in diameter. The spin rotator needs to have a focusing area of this size. The focusing area is defined as an area where electric and magnetic field distributions are expressed by Eqs. (2.7) and (2.8), or (2.12) and (2.13) with accuracy of ± 0.2 %, which have enough focusing effect to lead the electrons to the spin detector.

The focusing area could be enlarged by increasing the total size of the spin rotator. This approach, however, is not practical since the rotator size would be larger

than the SEM gun. We set the goal size of the spin rotator to be $50 \times 50 \times 50$ mm^3 which enables easy handling and easy adjustment without increasing the total size of the spin SEM.

Conventional Wien filters have been applied for a fine beam with a several-micrometer diameter such as in transmission electron microscopy. In our estimation their focusing areas are less than 1 mm^2 and do not satisfy our requirement. The spin rotator needs to be much improved in terms of the focusing characteristics by designing new shapes of electrodes and magnet pole-pieces. Since type 1 has been studied more in terms of focusing characteristics[8-10] we chose type 1 for our design here in order to take advantage of the previous technique as much as possible.

2.4 Design

2.4.1 Inside the spin rotator

Computer simulation was done to study the range of focusing area for various shapes of electrodes and magnet pole-pieces by using the differential equation solver language.[12] The fields are expected to be homogeneous along the z-direction inside the spin rotator, because the length of the spin rotator along the z-axis is long enough in comparison with the distances between the electrodes and the magnet pole-pieces. Therefore the calculation was two dimensional in the x-y plane, for simplicity.

The calculated results are shown in Figs. 2.2, where (a), (c) and (e) are

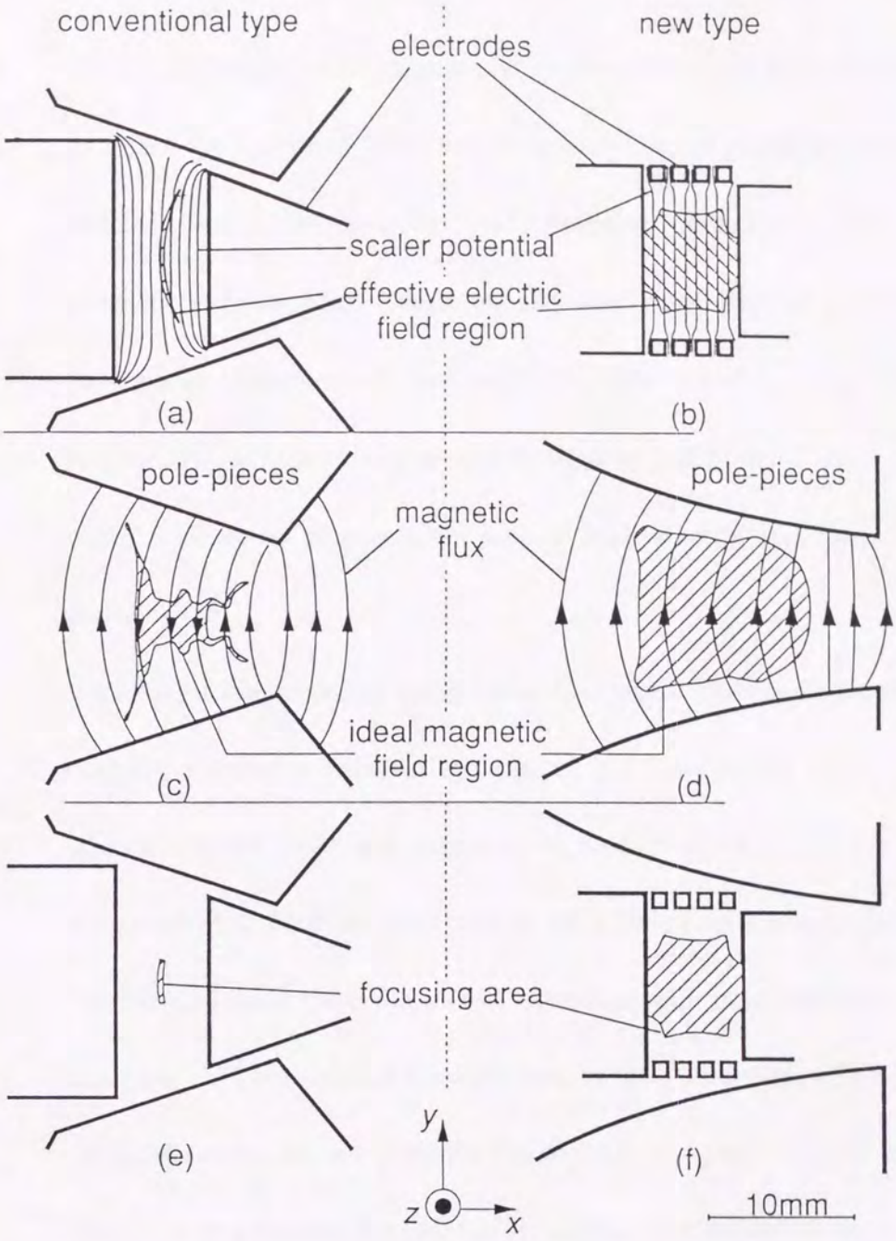

Fig. 2.2. Transverse (perpendicular to the optical axis) cross-sectional view of the calculated (a), (b) electric equi-potential planes and (c), (d) magnetic force lines and (e), (f) effective focusing area inside, (a), (c), (e) previously reported and (b), (d), (f) newly designed spin rotator. The hatched areas in (a)-(d) shows ideal field distributions and those in (e), (f) show effective focusing area necessary for stigmatic focusing. The pole-pieces are omitted in (b) and the electrodes are omitted in (c) and (d).[6]

calculations based on the previously proposed type[9] and (b), (d) and (f) are the newly proposed type. Figures 2.2(a) and (b) are the calculated electric equi-potential planes and the ideal electric field region with the electrodes. Figures 2.2(c) and (d) are the calculated magnetic force lines and the ideal magnetic field region with the magnet pole-pieces. Ideal electric and magnetic fields are defined by Eqs.(2.7) and (2.8), respectively, with accuracy of ±0.2 %. Figures 2.2(e) and (f) show the focusing area, which is obtained as a common area of ideal electric and magnetic fields obtained above.

As for electrodes in many cases, two pillars have been set as the positive and negative electrodes between the magnet pole-pieces. Between the two pillars the uniform electric fields are expected to be formed, however, they cannot produce completely flat equi-potential planes as a result of the edge effect (Fig. 2.2(a)). Therefore, Tsuno[9] showed a pair of electrodes with much narrower spacing in the x-direction, than the width of the electrodes in the y-direction, which decreases the edge effect. However, since the electrodes width in the y-direction is limited by the total size of the spin rotator, *i. e.*, 50 mm in our case, it is difficult to attain the effective area of 6 mm in diameter by Tsuno's method. We found out the ideal electric field region is, at maximum, as Fig. 2.2(a) shows, achieved as long as the electrodes are two pillars and their distance is kept at 6 mm.

Our approach is to use pairs of fine auxiliary electrodes in order to control the electric field distribution. The suitable number and the size of the auxiliary electrodes were investigated so as not only to produce a wide uniform electric field area but also

to have a simple and vacuum-discharge-free structure. We found that four pairs of auxiliary electrodes 1 mm thick and 1 mm wide as shown in Fig. 2.2(b) are enough to give a homogeneous electric field area 6 mm in diameter.

Previously proposed magnet pole-pieces[9] were shaped into a prism with tilted flat surfaces to approximate the magnetic field distribution expressed in Eq. (2.8). We studied the area of ideal magnetic field for various inclination angles of each plane, and obtained a configuration shown in Fig. 2.2(c) which gives the maximum area. The area, however, is still narrower than our requirement. From the ideal magnetic field distribution of Eq. (2.8), the ideal magnetic scalar equi-potential plane ϕ is calculated as

$$\phi = By(1+\frac{x}{2r}) . \qquad (2.14)$$

It is a hyperbolic line in the x-y plane. Since magnet pole-pieces are made of high permeability material such as permalloy, the surfaces will be one of the magnetic scalar equi-potential planes. Therefore, if the magnet pole-pieces are formed in a hyperbolic cylindrical shape as expressed in Eq. (2.14), the ideal magnetic field distribution would be attained. The magnetic field distribution between the magnet pole-pieces of this shape is shown in Fig. 2.2(d). Clearly the ideal magnetic field distribution is achieved over a 6-mm-diameter in the x-y plane, which is sufficient for our requirement.

Comparing the focusing area of Figs. 2.2(e) and (f), we can see that the new type has much wider focusing area than the conventional type and achieves our requirement.

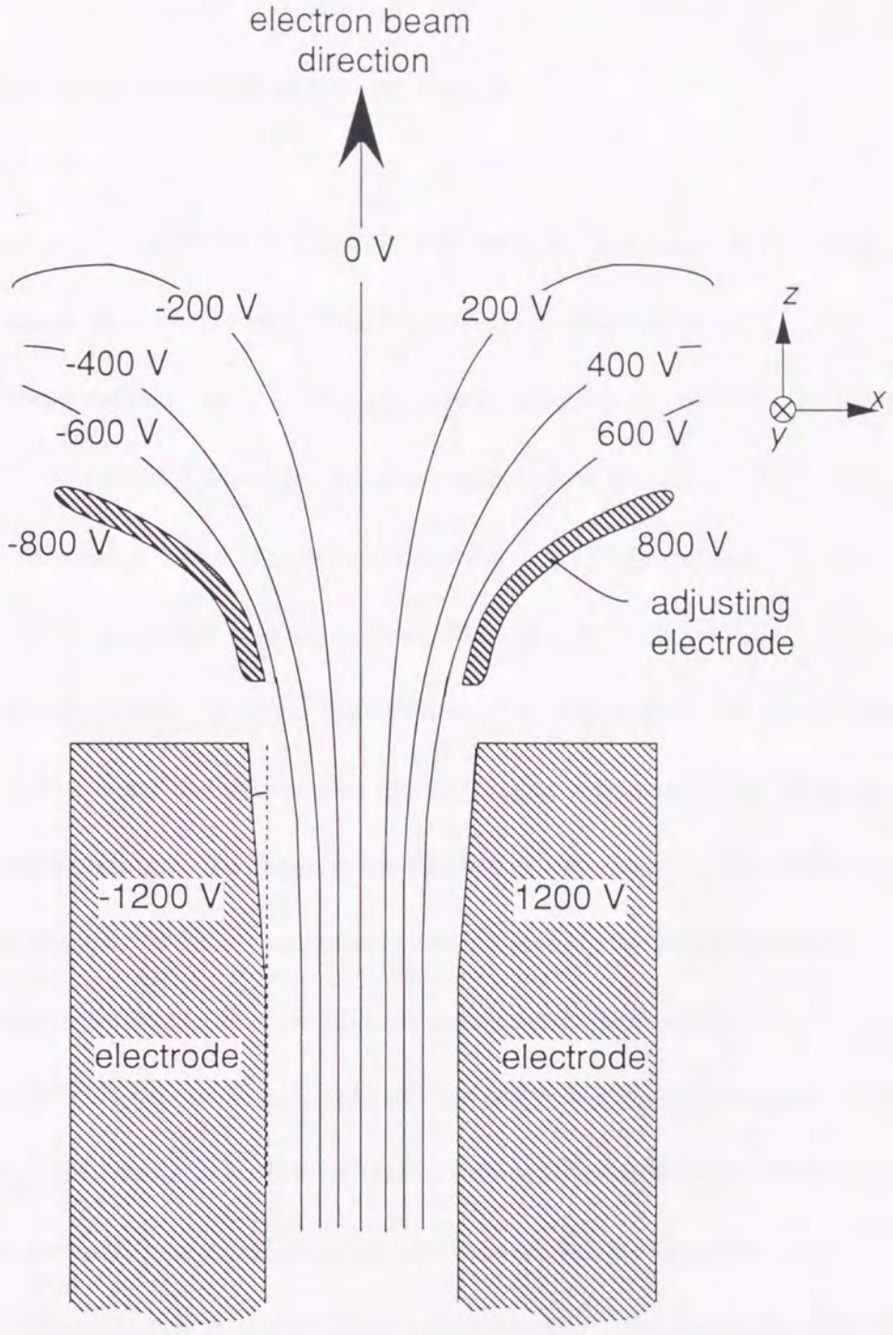

Fig. 2.3. Longitudinal (parallel to the optical axis) cross-sectional view of the calculated electric equi-potential planes at fringe regions of the spin rotator. This potential distribution satisfies the Wien condition necessary for straight electron movement.[6]

2.4.2 At the fringing regions of the spin rotator

The condition of Eq. (2.2) should be kept even at the fringing regions, which are around the entrance and the exit of the spin rotator as shown in Fig. 2.3, otherwise the electron beam deflects and the stigmatic focus would be destroyed. It is not easy, however, to adjust the fields at the fringing regions, since the fields change drastically in three-dimensional space. Tsuno[10] reported the spaces between the electrodes and those between the magnet pole-pieces should be equal to maintain Eq. (2.2) over the fringing regions. De Gryse *et al.*[13] reported another way where they put 13 pairs of auxiliary plates along the optical axis of the fringing regions in order to adjust the electric field accurately. We designed the spin rotator in which the space between the electrodes is narrower than that between the magneto-pole-pieces as shown in Fig. 2.2(f), which is preferable to make homogeneous electric fields inside the spin rotator. Therefore Tsuno's method is not applicable for our spin rotator. Moreover the space around the spin rotator is so limited that it is impossible to fix many extra auxiliary electrodes precisely before and after the spin rotator, like De Gryse's method.

Our approach was to take advantage of the auxiliary electrodes designed in the previous section. It is possible to adjust the fringing electric field to cooperate with the fringing magnetic field by extending auxiliary electrodes from inside the spin rotator and curving them to create the proper electric equi-potential planes.

For that purpose, first, the magnetic field distribution made by the magnet pole-pieces designed in the previous section was calculated along the z-axis by the

three dimensional simulation program by using an integral equation method.[14] To achieve the electric field distribution which satisfies the condition of Eq. (2.1) on the z-axis, we carried out computer simulation again. In the case of electric field, however, it is extremely difficult to calculate the three-dimensional electric field distribution, since there are 8 fine auxiliary electrodes in addition to the main electrodes. Thus we attained the required electric field distribution on the z-axis by two-dimensional field distribution, which is homogeneous in the y-direction, as described below.

The calculation result of the fringing electric equi-potential planes using the differential equation solver language[12] is shown in Fig. 2.3. The potential planes spread out at the fringing region. We put the adjusting electrodes in the fringing regions and tapered the edges of the main electrodes. By changing the shape and the voltage of the adjusting electrodes and the inclination angle of the tapers of the main electrodes by trial and error, the fringing electric fields with the ideal distribution were found. Here, ideal distribution was defined as the electric field which keeps the condition of Eq. (2.1) with the fringing magnetic field on the z-axis with an accuracy of ± 1 %, which is necessary to send all the secondary electrons to the spin detector. The fringing region is shorter than the rotator length, therefore large deflection or astigmatism is less possible in the fringing region, which eases the condition of the electric field in the fringing region compared to that in the inside region.

2.5 Building

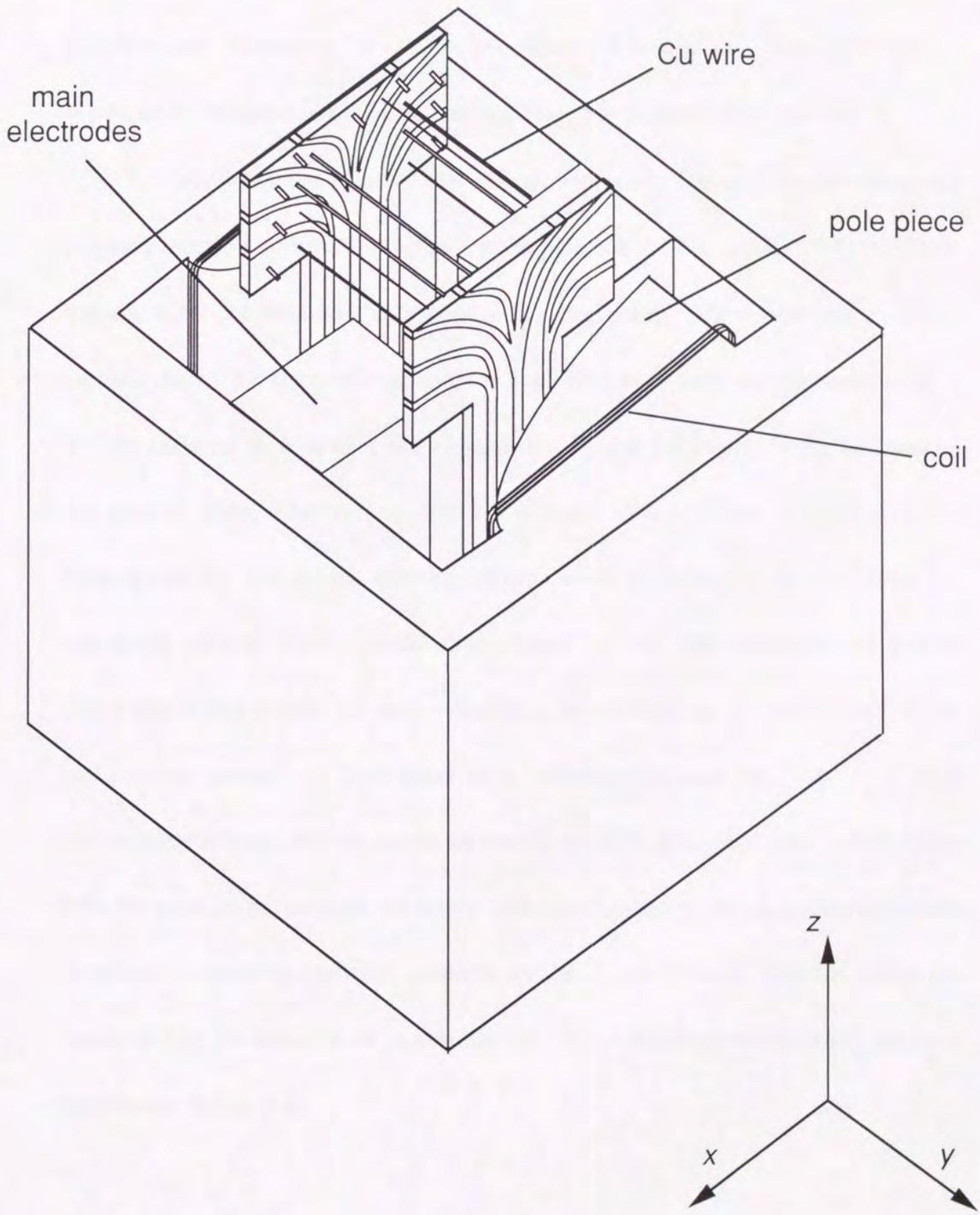

Fig. 2. 4. External appearance of the designed spin rotator. [6]

The external appearance of the designed spin rotator is shown in Fig. 2.4. The electron beam travels in the upper direction. The magnet pole-pieces are made of permalloy and shaped into a hyperbolic cylinder. The main electrodes are made of nonmagnetic material, titanium, so not to disturb the magnetic field distribution.

We calculated the electric field distribution inside the spin rotator supposing auxiliary electrodes shaped into fine square pillars as in Fig. 2.5(b). It is, however, difficult to set the electrodes accurately in the small space. Therefore Au patterns on a ceramic plate 1 mm thick take place of the fine pillars because it is much easier to print fine Au patterns on a ceramic plate accurately. Figure 2.5 shows the Au patterns on the ceramic plate. They run straight in the inside of the rotator, and curve at the fringing regions. The shapes of these patterns were determined so as to produce the calculated electric equi-potential lines shown in Fig. 2.3, where the adjusting electrodes shown in Fig. 2.3 were substituted by some of the Au patterns. Same Au patterns are printed on both sides of a ceramic plate and they have the same electrostatic voltage, so they can be an analogy to a fine pillar. The two ceramic plates with the same Au patterns are set facing each other, as shown in Fig. 2.4. Several pairs of points at mirror-symmetrical positions on the Au patterns on both the plates are connected by Cu wires, so as to simulate the two-dimensional electrostatic potential distribution in Fig. 2.3.

2.6 Performance Evaluation

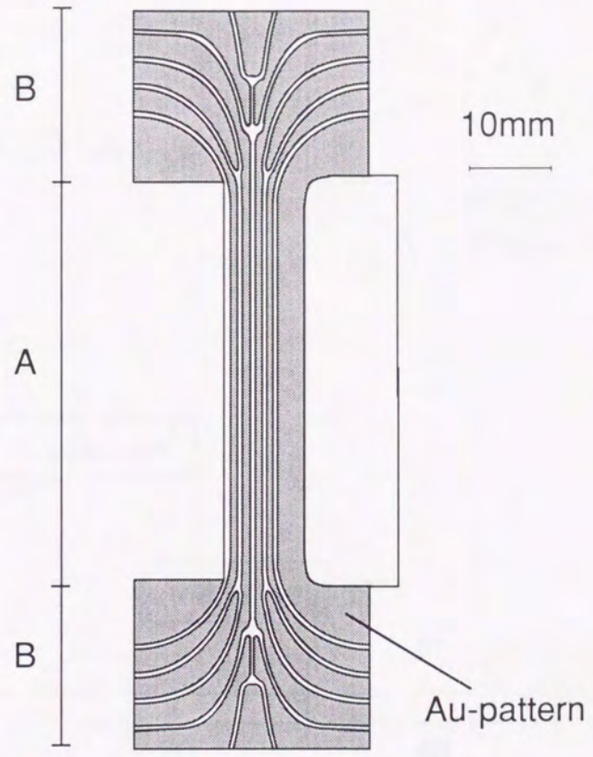

A : Inside the Wien filter
B : Outside the Wien filter

Fig. 2. 5. Auxiliary electrodes printed on a ceramic plate. [6]

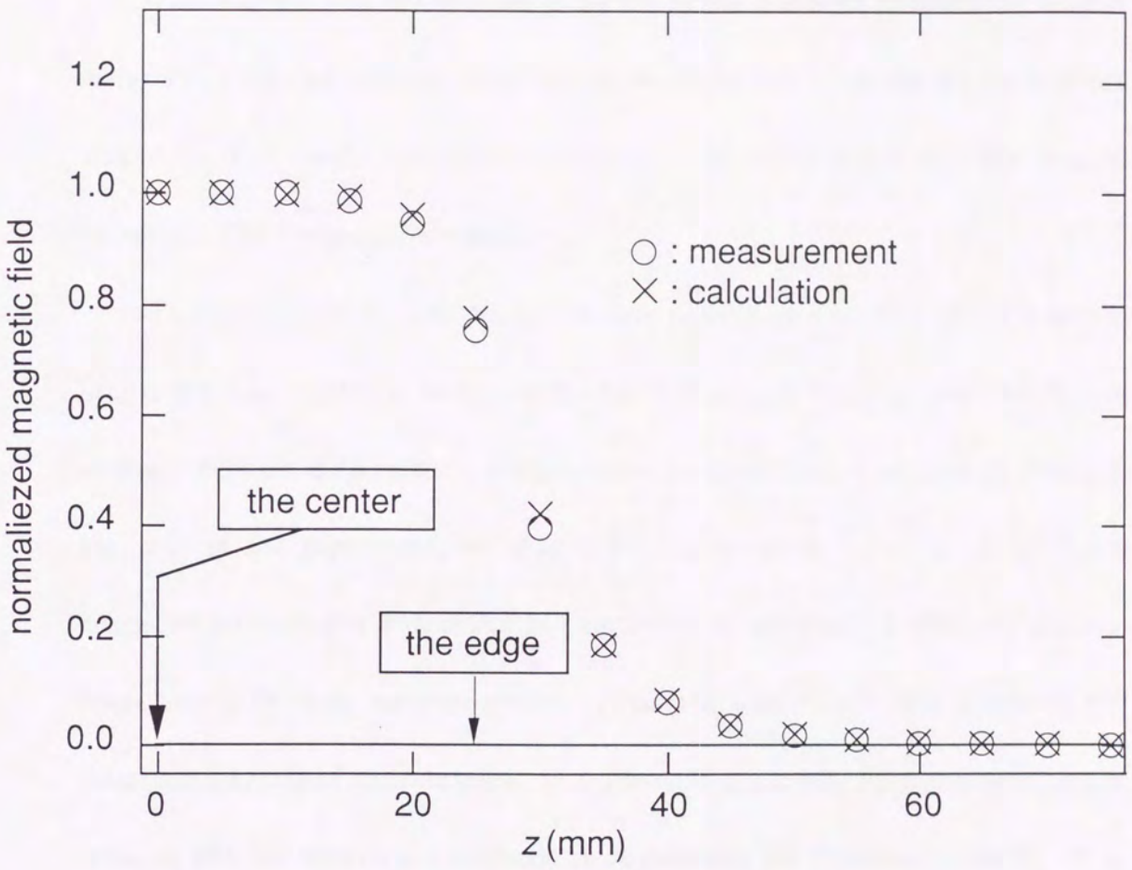

Fig. 2. 6. Distribution of th emagnetic flux density along the optical axis of the newly desighned spin rotator.[6]

The magnetic field distributions along the optical axis were measured by a gauss meter and compared with the calculated distributions to confirm the accuracy of our simulation. The results are shown in Fig. 2.6. The calculated results are in good agreement with the measured values.

To confirm that the polarization rotation angle is proportional to the magnetic field in the spin rotator as expressed by Eq. (2.3), and to calibrate the electric and magnetic field for $\pi/2$ rotation, we conducted an experiment shown schematically in Fig. 2.7. In the experiment, we used a Fe(001) plane as a sample of which the magnetization is in the x-direction and measured the polarization after the electron beam passed through the spin rotator. When the spin rotator is inactivated, the polarization vector of secondary electrons orients in the x-axis. When the spin rotator is active with the electric and magnetic fields satisfying the condition of the Eq. (2.1), the polarization rotates by α which is given by the Eq. (2.3). From Eqs. (2.3) and (2.5), the relation between the detected polarization component P_d and B is expressed as

$$P_d = P_x \cos(\frac{le}{vm} B) . \qquad (2.15)$$

Therefore the detected polarization should be expressed by a cosine function of the magnetic flux density, and when the magnetic field rotates the polarization by $\pi/2$, P_d should becomes zero.

Figure 2.8 shows the relation between B and P_d / P_x. It is clear that P_d is a cosine function of B. From the point $P_d = 0$, the magnetic field of $\pi/2$ rotation is determined to be 42 Oe. From the calculated magnetic field distribution shown in Fig. 2.6, the

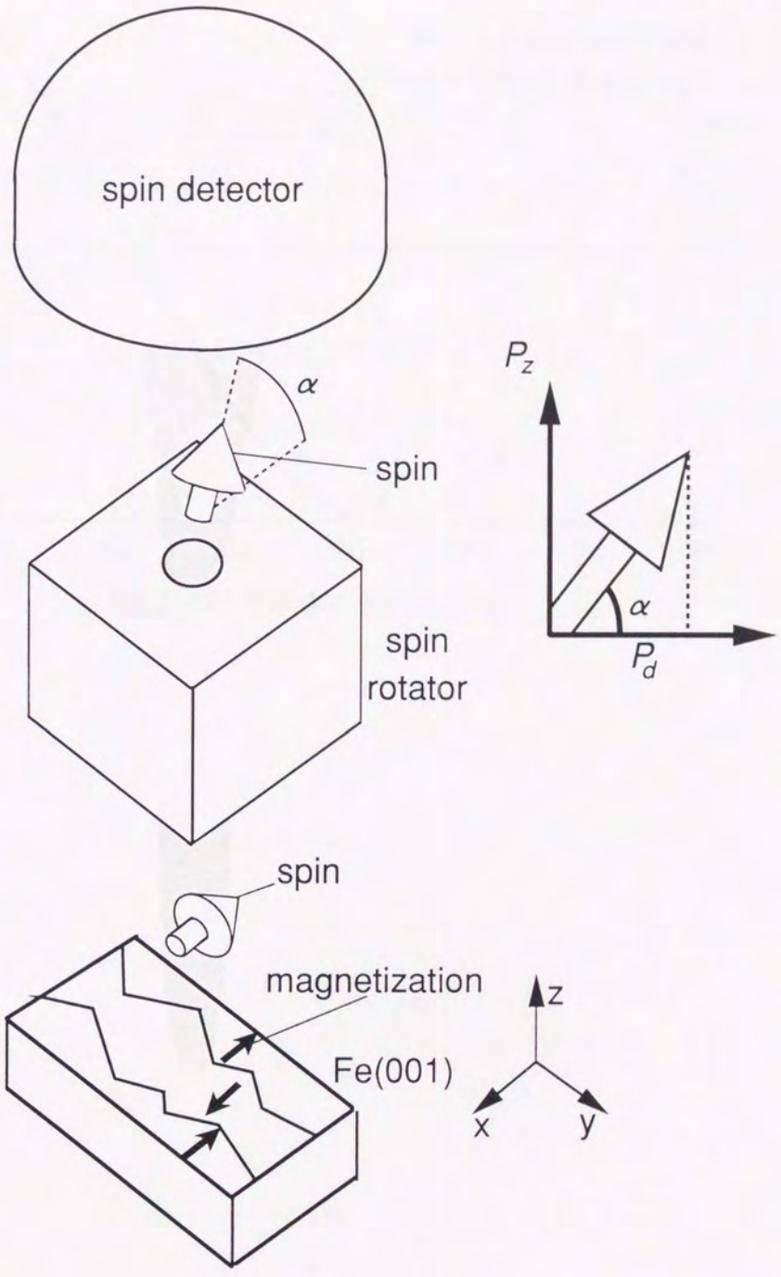

Fig. 2. 7. Schematic of the performance examination of the spin rotator. [6]

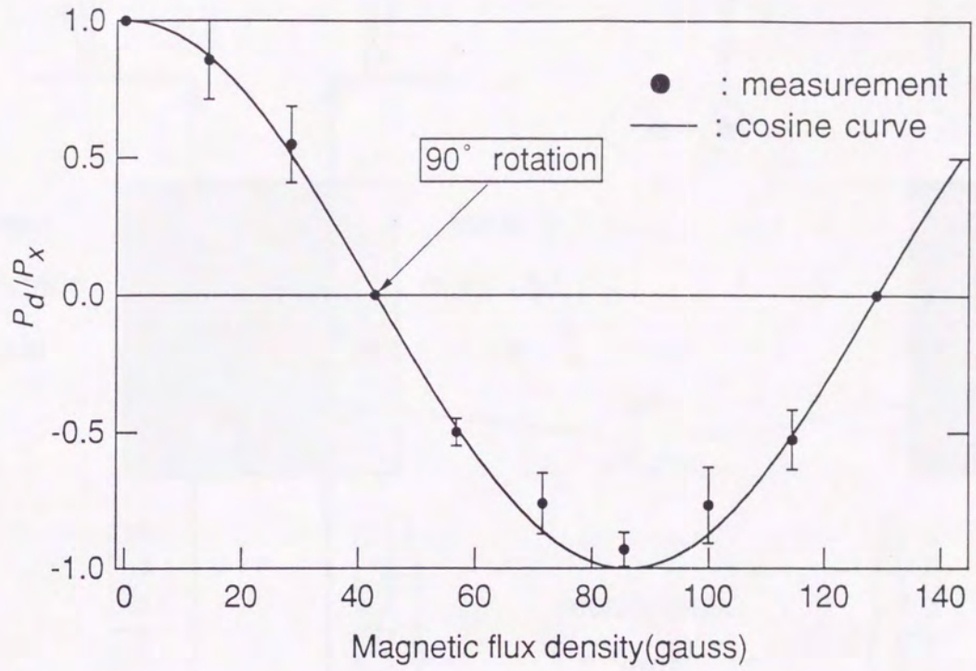

Fig. 2. 8. Magnetic field dependency of the polarization component P_d normalized by P_d=P_x at zero mangetic field after passing through the spin rotator[6]

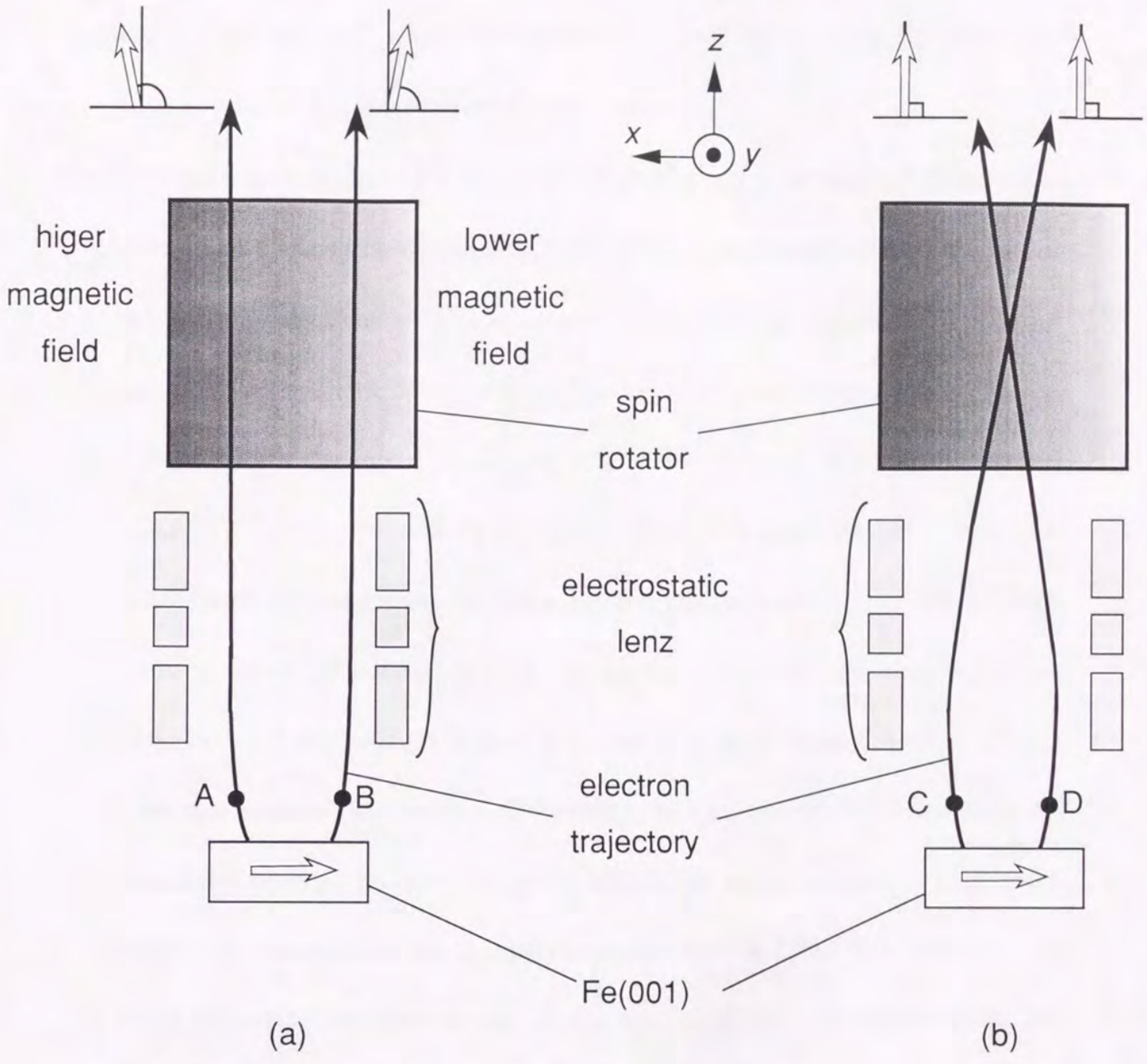

Fig. 2. 9. Schematic diagram showing trajectory dependent spin rotation (a) and its correction (b). The magnetic field increases from right to left in the spin rotator. In (a) electrons A and B pass through the higher and lower magnetic field regions respectively and suffer different spin rotation. In (b), the magnetic field integrated over the trajectories of electrons C and D are almost the same and so are the spin rotation[6]

magnetic field for $\pi/2$ rotation is estimated to be 40 Oe by using Eq. (2.2). This experimental result is close to the calculated value.

Next, we considered the dispersion of rotation angle. Scheinfein[15] theoretically showed that a homogeneous magnetic field gives a homogeneous rotation for various trajectories of electrons in the spin rotator, in the first order approximation. In our case, however, magnetic field is a linear function of the position as expressed by Eq. (2.8). Therefore the rotation angle depends on the electron trajectory in the spin rotator. Figure 2.9 schematically shows this effect. In a spin SEM, the samples are scanned with a primary beam, and the secondary electrons are emitted from different points on the sample and pass through a different regions in the spin rotator. Thus as shown in Fig. 2.9(a) electron A passing through the higher magnetic field region has larger spin rotation than electron B. However, we can minimize the inhomogeneous rotation by adjusting the electron optics so that the secondary electrons cross the optical axis at the middle of the spin rotator as shown in Fig. 2.9(b). The electron C (D) senses larger (smaller) magnetic field on the former half way in the spin rotator and senses smaller (larger) magnetic field on the latter half. As a result, the integrated magnetic fields which both of the electrons sense become almost the same. The electron trajectory shown in Fig. 2.9(b) can be easily attained by adjusting the strength of the electrostatic lens before the spin rotator. To confirm this consideration, we measured polarization emitted from a 1-mm area along the x-direction for different lens strengths. The results are shown in Fig. 2.10. The rotation does depend on the emission points of the secondary electrons. The dependency, however, could be

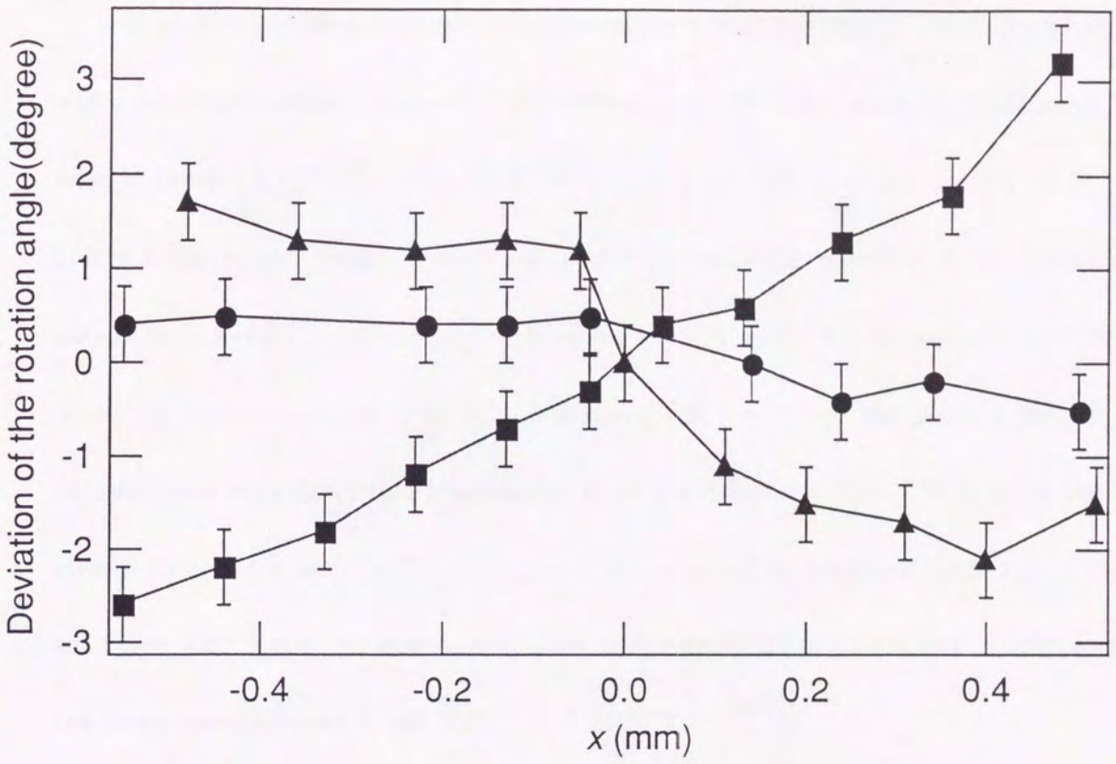

Fig. 2.10. The emission position dependency of the secondary polarization vector rotation for three different strengths of einzel lens in front of the spin rotator. The lens becomes stronger in order of ▲, ●, ■. The situation of ▲ and ● corresponds to (a) and (b) of Fig. 2.8, respectively.[6]

minimized within 1 degree by adjusting the strength of the einzel lens set just before the spin rotator.

In order to confirm that the spin rotator has a focusing area of 6-mm diameter and a magnetic domain image of 1-mm diameter can be taken using it, a magnetic domain image of GdFeCo, was taken in low magnification as shown in Fig. 2.11. GdFeCo has an easy magnetization axis in the perpendicular direction to the sample surface and used for magneto-optical recording medium. In the figure, many domains of about 40 micrometers are seen with black and white contrast where black (white) domains have the polarization components in the down (up) direction. The domains are clearly observed within the 1-mm-diameter region which is expressed by the oval in the figure. This means the spin rotator has a wide area of focusing capability enough for the secondary electrons in spin SEM.

Figure 2.12 shows another example which demonstrates the performance of our spin rotator. The sample is a TbFeCo magneto-optical disk with recorded marks.[16] This material has an easy magnetization axis perpendicular to the surface. Previously we observed the magnetization distribution in a similar kind of sample.[17] Here we used a newly developed spin SEM[18] with higher spatial resolution. The recorded marks are clearly observed. In the next chapter we explain the observation results of the recorded marks of this magneto-optical recording material TbFeCo in detail.

2.7 Conclusion

Fig. 2. 11. The magnetic domain images of GdFeCo obtained by using a magnetization component normal to the sample surface. The oval shows the 1-mm-diameter area. [6]

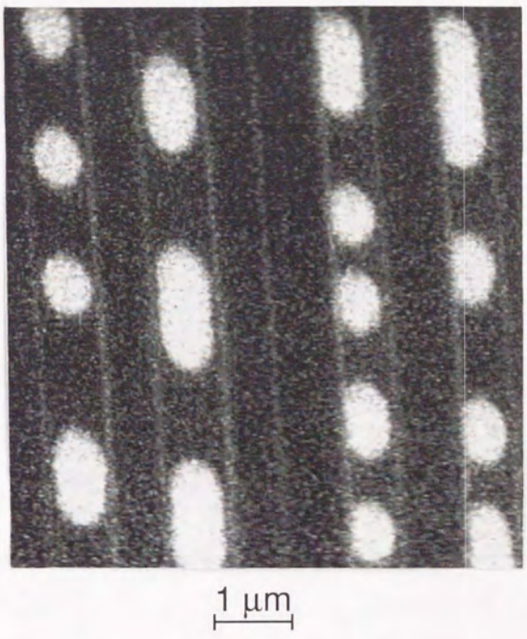

Fig. 2. 2. The magnetic domain images of magneto-optically recorded TbFeCo obtained by using a magnetization component normal to the sample surface. [6]

A spin rotator was developed in order to be installed in our spin SEM and detect the magnetization component perpendicular to the sample surface. The basic structure of the spin rotator is same as a well-known energy filter named a Wien Filter, but its focusing area was enlarged by using hyperbolic cylindrical pole pieces as a magnet and several auxiliary electrodes which satisfies the condition for working as the spin rotator in our spin SEM. We examined the performance and confirmed our spin SEM can detect all three magnetization components of the sample.

references

[1]J. Unguris, M. R. Scheinfein, D. T. Pierce, and R. J. Celotta, Appl. Phys. Lett. **55**, 2553 (1989).

[2]H. P. Oepen and J. Kirschner, Scanning Microscopy **5**, 1(1991).

[3]M. Aeschlimann, M. R. Scheinfein, J. Unguris, F. J. A. M. Greidanus, and S. Klahn, J. Appl. Phys. **68**, 4710 (1990).

[4]E. Kisker, G. Baum, A. H. Mahan, W. Raith, and B. Reihl, Phys.Rev. **B.18**, 2256 (1978).

[5]T. Duden and E. Bauer, Rev. Sci. Instrum. **66**, 2861(1995).

[6]T. Kohashi, H. Matsuyama, and K. Koike, Rev.Sci.Instrum. **66**,5537(1995).

[7]W. Wien, Ann. Phys. **65**, 444 (1898).

[8]R. L. Seliger, J. Appl. Phys. **43**, 2352 (1972).

[9]K. Tsuno, M. Terauchi, and M. Tanaka, Optik **80**, 149 (1987).

[10]K. Tsuno, Optik **89**, 31 (1991).

[11]W. Legler, Z. Physik **171**, 424(1963).

[12]Y. Umetani, M. Tsuji, and K. Iwasawa, Proc. IFIP TC2/WG2.5, 147 (1985).

[13]R. De Gryse, J. P. Landuyt, G. Vervaet, and J. Vennik, J. Phys. **E 10**, 458 (1977).

[14]M. Koizumi, IEEE Trans. Magn. **MAG-27**, 4079(1991).

[15]M. R. Scheinfein, Optik **82**, 99(1989).

[16]M. Takahashi, H. Sukeda, M. Ojima, and N. Ohta, J. Appl. Phys. **63**, 3838 (1988).

[17]T. Kohashi, H. Matsuyama, K. Koike, and H. Miyamoto, J. Mag. Soc. Jpn. **18**, Suppl.,

No.S1, 7(1994).

[18]H. Matsuyama, K. Koike, J. Electron Microsc. **43**, 157(1994).

3. Observation of Recorded Marks on Magneto-Optical Recording Media TbFeCo

3.1. Introduction

The recorded mark shapes and sizes in magneto-optical recording media are of considerable importance in data storage. The success of magneto-optical recording depends on the reliable and repeatable reversal of magnetization in a micron-sized area. To achieve higher density in magneto-optical recording, smaller uniform marks should be recorded precisely in narrow tracks, avoiding mark shape irregularity that decreases carrier-to-noise (C/N) ratio, and the cross write, in which the marks extend into the adjacent tracks.

In this chapter we report two studies of the recorded mark shapes of the magneto-optical medium TbFeCo.[1] In the first study[2] we determined the laser power dependency of mark shapes and sizes in a land/groove recording.[3] This work is for improving high density recordings because the track pitch becomes small in land/groove recording, the cross write is thought to be a serious problem, as well as cross talk and cross erase.

Several observations of magnetized domains on grooved substrates have been reported[4,5] and a phenomenon has been observed in which the written marks on the grooved substrate do not expand across the borders between lands and grooves. Kesteren *et al.*[4] observed the phenomenon for marks on CoPt film prepared on a V-grooved substrate using magnetic force microscopy (MFM). However, CoPt, which is

studied as the magneto-optical medium of the next generation,[6] has different characteristics from TbFeCo, which is currently used as a magneto-optical medium. Gadetsky *et al.*[5] observed this phenomenon of TbFeCo film in the field-induced magnetization reversal process on the grooved substrates and in thermomagnetically recording on the patched substrate by using a polarized-light microscope. To investigate the cross-writing effect of land/groove recording more detail, we need to observe marks recorded under actual condition. In this study we observed marks recorded thermomagnetically on both lands and grooves of TbFeCo film.

Our second study[7] describes the relation between the mark shapes for TbFeCo recording film and its underlayer-roughness, which were prepared on V-shaped grooves. Previously, Ushiyama *et al.* reported[8] that the shapes of the recorded marks tend to be uniform on the rough underlayer though they are more irregular on the smooth underlayer, which are closely related with the noise characteristics. In this study, we investigated the role of the underlayer-roughness in forming the mark shapes. We observed the applied field dependencies of the mark shapes on TbFeCo films on both the smooth and the rough underlayers. The relation between the recording characteristics and the magnetization reversal process of these two media is discussed.

Spin SEM is especially useful for this kind of study because it can detect magnetization information independent of sample surface topography. Thus, it is useful for investigating samples with uneven topographies such as a magneto-optical medium on a grooved substrate, or an underlayer with surface roughness.

3.2 Experiment

TbFeCo recording films were prepared by magnetron sputtering. We used a pregrooved glass-substrate (direct-etched) for the land/groove substrate of our first study. The disk structure is shown in Fig. 3.1. Nitride underlayer (85 nm), TbFeCo (80 nm), and Al alloy overcoating layer (10 nm) were prepared on the substrate. Marks were recorded on both lands and grooves using a magneto-optical drive whose objective lens has a numerical aperture of 0.55, and a laser with a wavelength of 680 nm. In this experiment, we changed laser powers track by track so that we could easily observe the laser power dependency in one spin-SEM image. Each mark had a length several times the nominal unit length of 0.3 μ m for mark-edge recording.[9] During the recording process mark widths were adjusted at a constant by multi-pulse recording with preheating power[10] where the mark length is controlled by number of the pulses as shown in Fig. 3.2.

In the second study we used glass substrates pregrooved with photo-polymerized (2P) resin. The track pitch was 1.4 μ m. Nitride underlayer (85 nm), TbFeCo (25 nm), and Al alloy overcoating layer (10 nm) were prepared on the substrate. We made two kinds of samples with the SiN underlayer having different surface roughness, as we did in our previous work.[8] The marks were recorded using a magneto-optical drive whose objective lens has a numerical aperture of 0.55, and a laser with a wavelength of 830 nm.

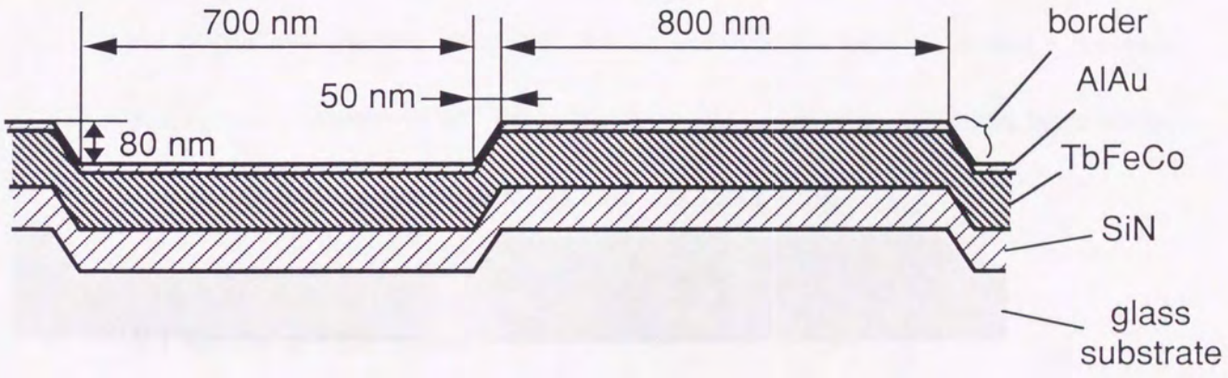

Fig. 3. 1. The structure of the magneto-optical medium used in the first study. [2]

We used 10-nm thick Al alloy layers for overcoating layers of all samples instead of 60-80 nm-thick nitride layers which are generally used for the TbFeCo medium. During the spin SEM measurements, images represent magnetization of a 1 nm thick surface region and the overcoating layer is removed by Ar-ion bombardment before measurement. In this sense the thinner overcoating layer of Al alloy can be removed over a shorter period, saving considerable experimental time.

The samples were cut into small pieces of about 10×10 mm^2 and put into the spin SEM chamber. After sample-surface cleaning by Ar^+-ion bombardment and getting rid of the overcoarting layer, the domain observations were made under the base pressure on the order of 10^{-7} Pa. In the spin SEM observation, the probe beam energy was 15 keV and the typical probe current was about 1 nA.

3.3 Results and Discussion

3.3.1 The marks on the land/groove substrate

Figures 3.3 show the domain images of recorded marks of TbFeCo on lands (a) and grooves (b), and Fig. 3.4 shows a higher magnification image of marks on grooves recorded using low laser power. The contrast is dependent on the magnetization component perpendicular to the surface of the sample. In these figures the laser beam runs from left to right.

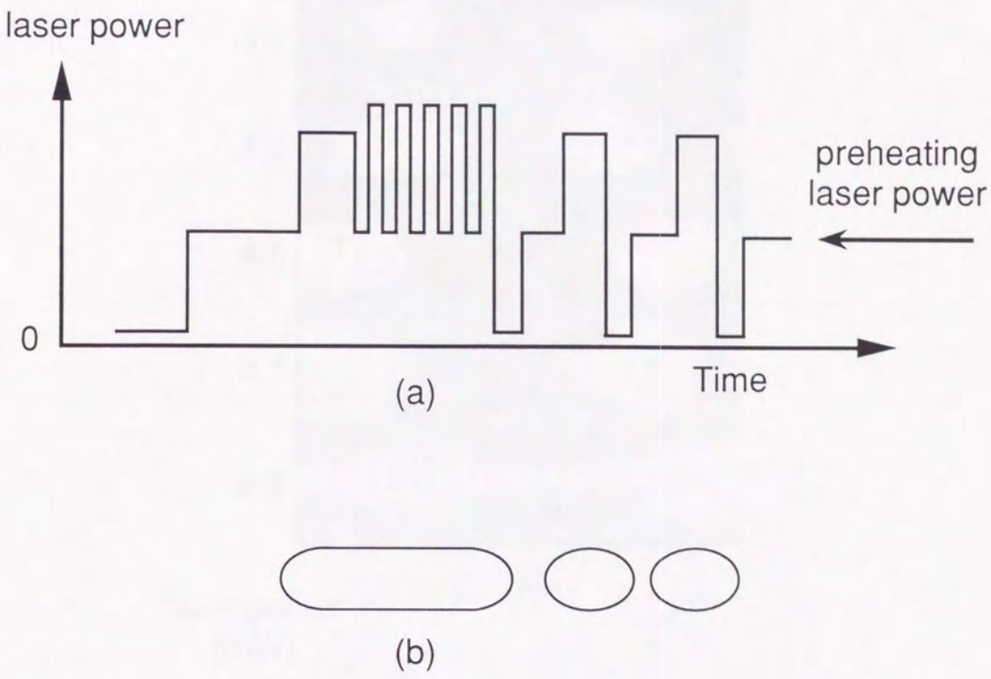

Fig. 3. 2. (a)Write laser wave form, and (b)shape of the recorded marks. [7]

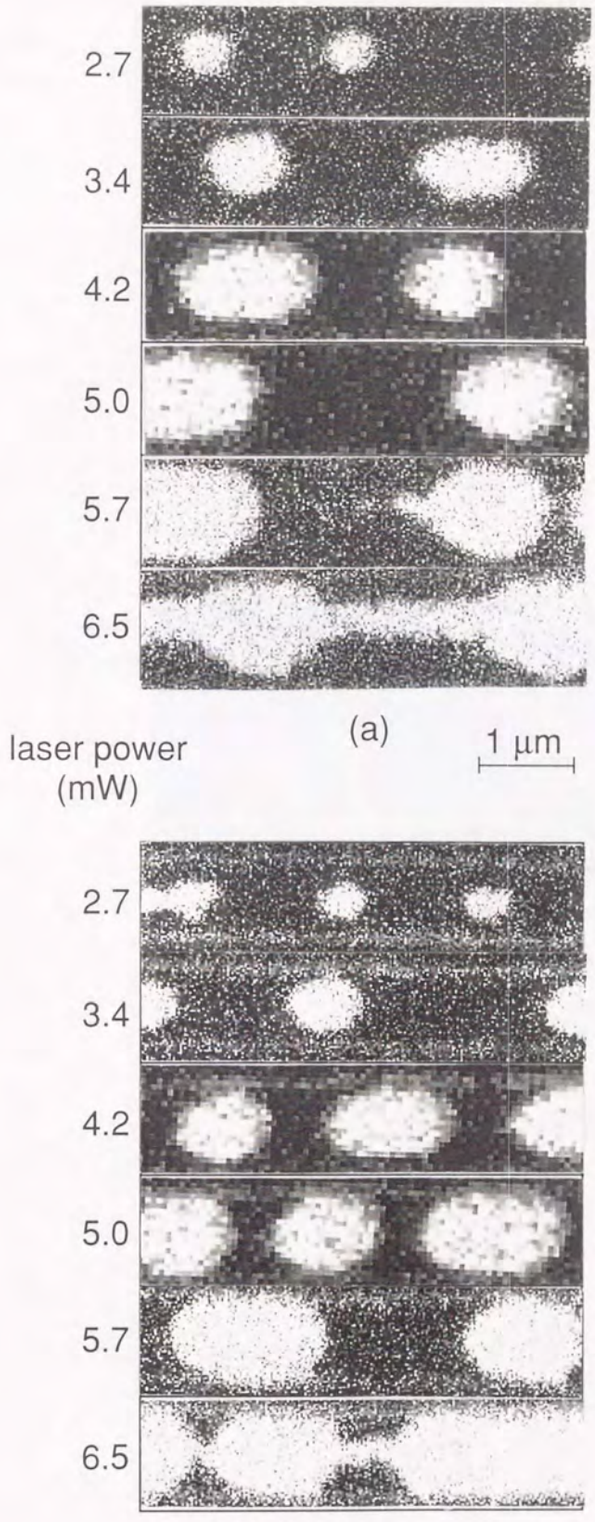

Fig. 3. 3. Recorded marks of TbFeCo on lands (a), on grooves (b). [7]

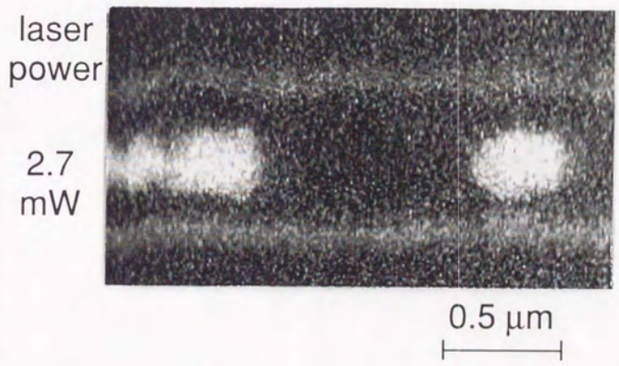

Fig. 3. 4. A high magnification image of marks recorded by low laser power on a groove. [7]

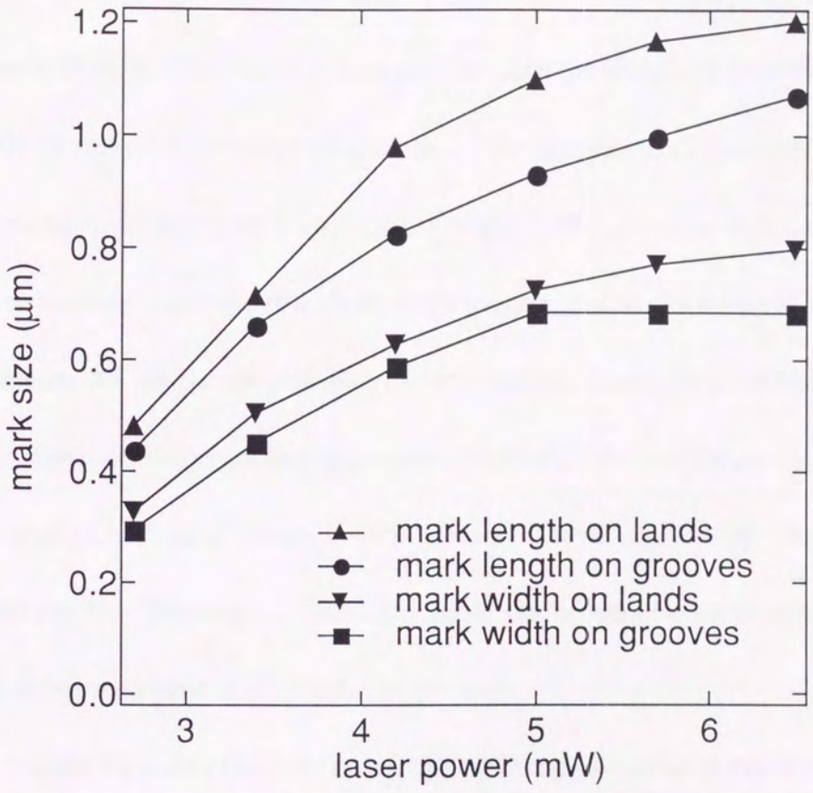

Fig. 3. 5. The laser power dependency of the recorded mark sizes. [7]

In Figs. 3.4 (a) and (b), various lengths of recorded marks as used in the mark-edge recording are observed. Because of the multi-pulse recording[9] as shown in Figs. 3.2, the widths of the marks are almost the same in each track and are independent of the mark lengths. The shapes are almost the same for lands and grooves and sizes are slightly larger on lands than on grooves. This suggests that coercivity is larger on grooves than on lands. At a laser power of 2.7 mW tiny marks with distorted shapes were observed on grooves (Fig. 3.4), while oval-shaped marks were recorded on lands. This means 2.7 mW is not sufficient to form uniform domains against the coercivity on the grooves. As the recording laser power increases the mark sizes become large. In the region of high laser power, even a preheating laser created tail-like irregularities. In addition, the side edges of marks are flat at the borders between lands and grooves, which is more obvious in the marks on grooves.

Figure 3.5 shows the laser power dependencies of average sizes of marks (some of which are not shown in Figs. 3.3), with shortest nominal length. The mark sizes, except for the mark width on grooves, increase with the laser power as previously reported.[11,12] In thermomagnetical recording, the area of the magnetization reversal depends on the temperature distribution created by the laser, and higher laser powers can create larger marks. On grooves, however, mark width seems to saturate with a value of 0.7 μ m around 5 mW while mark length continuously increases. In this region, the widths of marks already reach the width of the track and side edges of marks flatten along the border lines as Fig. 3.3(b) shows. This means that marks do not extend into adjacent tracks and mark width saturates even when laser power is high enough. The effect is

not very clear in marks on lands, where mark sizes increase monotonously both in width and length as laser power increases. This is because the land width 0.8 μ m is wider than that of grooves, and laser power is not sufficient to saturate mark width. However, as Fig. 3.3(a) shows, the upper edges of the sides of marks have already reached the borders of grooves and flattened in the region of the high laser power, where marks were not recorded at the exact centers of tracks. Mark width is limited by track width and marks cannot expand to adjacent tracks.

Borders between lands and grooves seem to prevent recorded marks from expanding to adjacent tracks. In other words, the borders stop the magnetization reversal process, which was reported by Gadetsky *et al.*[5] There are several possible factors for this phenomenon. Gadetsky *et al.* suggested that one of those factors may be the difference in the coercivities of grooves and lands. Larger coercivity on either lands or grooves stops the wall motion on the other with smaller coercivity. In our experiment, however, this prevention is also occurred to the mark expansion from the grooves where the coercivities are larger, to the lands where the coercivities are smaller. Therefore the difference of the coercivities is not crucial element in our experiment.

Gadetsky *et al.* suggested another factor: that the borders themselves have the pinning effect. The simulation[13,14] shows the presence of spatial variation in the magnetic parameters of the material, such as anisotropy energy, affects the pinning force. In Figs. 3.3 and 3.4, the color at the borders is gray, which means the perpendicular magnetization component at the border is smaller than that on the other

areas of the lands and grooves. This agrees with the previous work[5] which confirmed that the anisotropy axis at the borders directs to the different direction from those at other areas due to the difference of the surface inclination angles. Therefore the magnetic characteristics are different such as in the anisotropy between the borders and the other areas, and the prevention of the wall motion may be caused by the pinning effect related with the magnetic characteristics at the borders.

The thermal conductivity at the borders must also be considered since we recorded the marks thermomagnetically. The film thickness at the borders must have a tendency to be thinner than that on the other areas in the sputtering because of the surface inclination. This causes a decrease in the thermal conductivity and the mark expansion might be prevented in the thermomagnetic recording at the borders. As described above, there are several possible causes why the wall motion is stopped and further experiments are needed to explain the mechanism of the pinning.

This stopping of the wall motion is useful because we can keep recorded marks within tracks even if the laser power exceeds the proper value to some extent. This means that borders increase the laser power margin for recording. We can say that cross write, which has been considered to be a serious problem in land/groove recording, rarely happens in this kind of magneto-optical medium.

3.3.2 The marks on the rough and smooth underlayer

Previously we studied the underlayer roughness dependency of the noise characteristics.[8] By smoothing the underlayer surface the noise of the non-recorded state can be decreased, whereas the noise level of the recorded state does not change very much. This means the recording noise, which is defined by subtracting the noise of the non-recorded state from that of the recorded state, is increased by smoothing the underlayer surface. This is explained by the difference in the mark shapes recorded on both smooth and rough underlayers, which were observed by spin SEM. The mark shapes on the smooth underlayer are irregular, but, those on the rough underlayer are more uniform. This can be explained if we assume more wall pinning sites for rough underlayer than for smooth one, as Satoh *et al.* suggested.[15] Since a domain wall stops at a pinning site the mark shape tends to be polygon connecting the pinning sites. Thus the domain shapes become more irregular in the film with fewer pinning sites. Satoh *et al.* also presumed that the magnetization reversal process depends on the underlayer roughness because of the difference in the number and the force of the pinning sites, which are related with the recording characteristics.

In the present study we observed marks recorded with various values of the field opposite to that of normal recording in order to study the role of the underlayer roughness in forming the recorded marks.

Figure 3.6 shows the mark images recorded under the various external fields from -150 to 0 Oe on the smooth underlayer. Figures 3.7 show the mark images recorded under the fields from -400 to 0 Oe on the rough underlayer (a), and higher magnification images of marks on the rough underlayer (b). The minus sign indicates

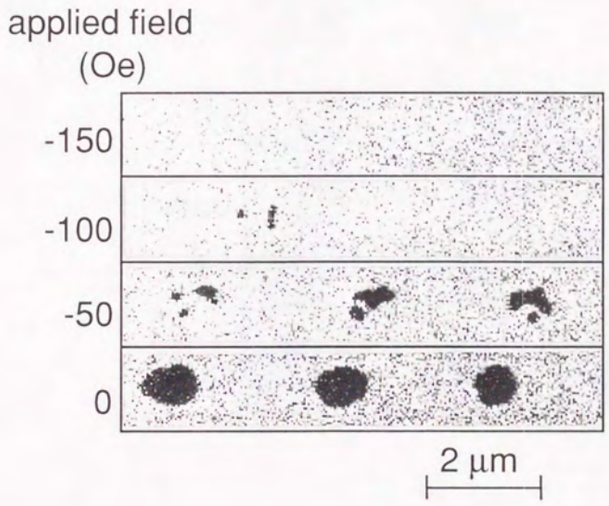

Fig. 3. 6. The mark images of TbFeCo recorded in the zero or negative magnetic fields on the smooth underlayer.[7]

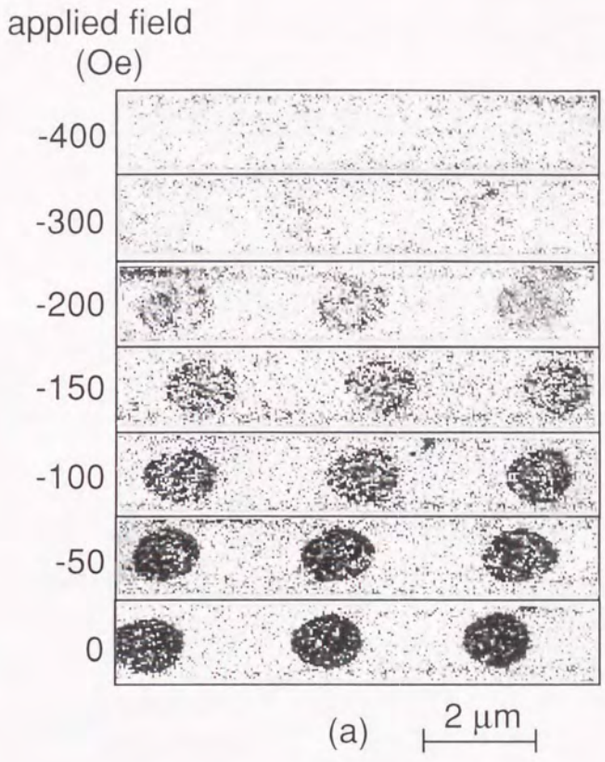

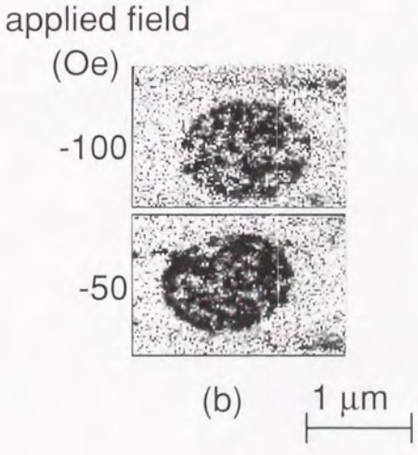

Fig. 3. 7. The mark images of TbFeCo recorded in the zero or negative magnetic fields on the rough underlayer (a) and some higher images of them (b). [7]

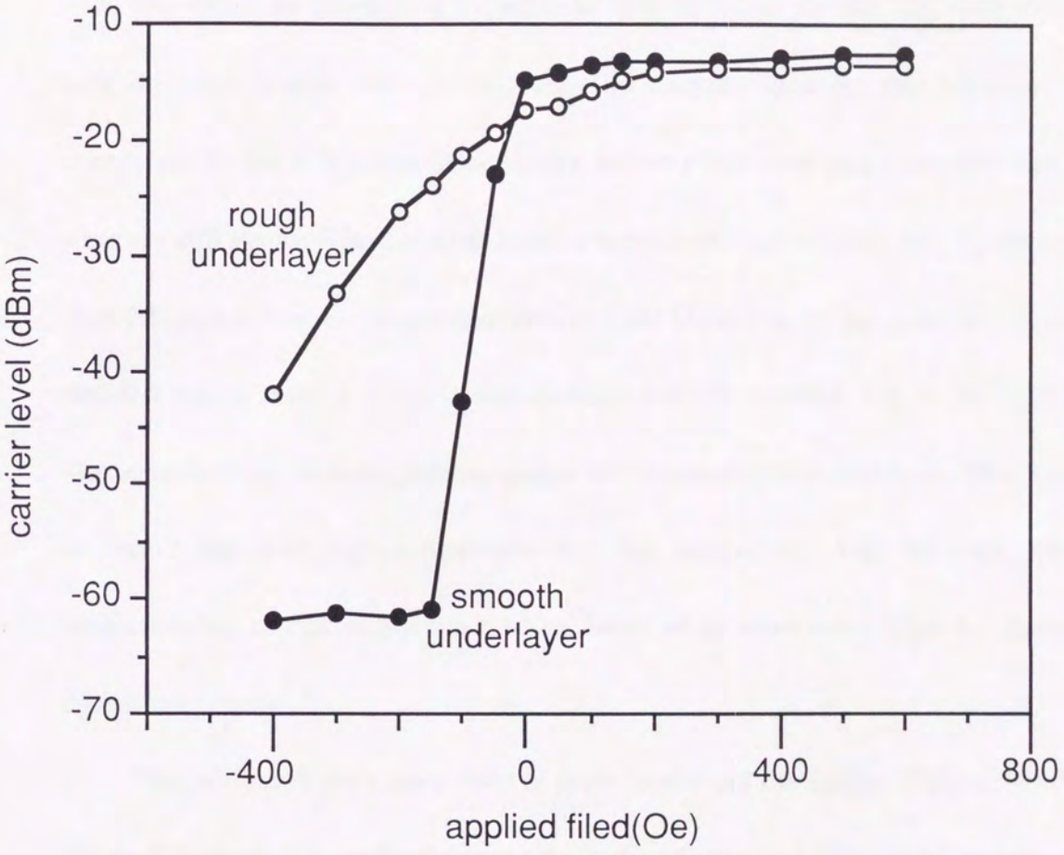

Fig. 3. 8. The external field dependency of the carrier level of TbFeCo recorded on the rough and the smooth underlayer.[7]

that field direction is opposite to that of normal recording, however, magnetization reversal occurs because of the demagnetization fields. Apparently the process of the mark creation is different in Figs. 3.6 and 3.7. In Fig. 3.6 no domains are recorded at -150 Oe. When the strength of the external field decreases to -100 Oe small domains with distorted shapes are created, and the domains grow as the negative field decreases. At the 0 field the mark shapes almost reach their usual one although the sizes are still smaller. On the other hand, a number of small domains with a size of less than 0.1 μ m appear at the negative field of -300 Oe in Fig. 3.7(a). It should be noted that the complete mark shape is already formed in the negative field of 200-300 Oe. The number of the small domains increases as the negative field decreases. This is clear in Fig. 3.7(b) with higher magnification. The images at -100 Oe show similar characteristics to the images reported by Satoh *et al.* which were taken by polarized optical microscope.[15]

The relation of the carrier level of these media and the applied field was studied. Figure 3.8 shows the same tendency reported by Satoh *et al.* This is consistent with the result of the mark images. For both samples the carrier keeps almost constant when the marks were recorded under the positive applied field. On the rough underlayer the carrier decreases gradually as the negative field increases and it reaches the noise level at -300 Oe. In contrast, on the smooth underlayer the carrier level decreases drastically around -50 Oe and reaches the noise level.

Given these results, the magnetization reversal process can be explained by using the assumptions of Satoh *et al.*[15] As for the case with the smooth underlayer as

shown in Fig. 3.6, in the higher negative field region than 150 Oe, no domains can be observed. One explanation for this is that tiny reversed multidomains, which have nucleated once during the thermomagnetic recording process, collapse instantaneously after the laser beam goes away. This is because the force to shrink the domain overcomes the force to expand and wall-pinning force, where the force to shrink and expand the walls comes respectively from the wall energy and the demagnetization energy. When the force to expand walls overcomes other forces during the laser heating in the higher field region, in our experiments the region of the negative field with less strength than 50 Oe, the reversed domains expand rapidly, positioning the walls to the pinning sites, and are stable after the laser heating. The number of the pinning sites should be small judging from the ragged shapes in the region of negative field of 50 Oe.

In Fig. 3.7, on the other hand, tiny domains, nucleating during the laser heating, can exist stably after the laser heating due to the strong force of the pinning sites. It is difficult for the force to expand walls to overcome the pinning force, so the size of each domain does not grow largely as the negative field decreases, whereas the number of small domains increases. Thus it is reasonable to say that more pinning sites with stronger pinning force exist in this film than that in Fig. 3.6. The small domains form the mark shapes at the field of -200 Oe, which does not become much larger as the field increases. The size of the recorded mark on this sample, therefore, is not sensitive to the external field, which is supposed to be due to the sharp decrease of the coercive force at the mark edge when it is thermomagnetically recorded.[11] To explain this

insensitivity precisely, however, other factors - such as the demagnetization field from the close reversed domains or the spatial variation of the coecivity force - must be taken into account.

The pinning force may be caused by the spatial variation of the magnetic parameters such as anisotropy due to the underlayer roughness, which is suggested by the simulation.[13,14] Further experiments are required to study the position where the domain walls are pinned on the uneven sample surface.

This difference in the magnetization reversal processes is supposed to be caused by the difference in the number and intensity of the wall pinning sites as discussed above. On the smooth underlayer with fewer pinning sites, the mark shapes become irregular, while they are uniform on the rough underlayer with more pinning sites. We can assume that the domain wall pinning sites are needed to create the uniform mark shapes and to decrease the recording noise.

3.4 Conclusion

The recorded mark shapes of magneto-optical media TbFeCo were studied. In the marks on the land/groove substrate, we confirmed that the borders between lands and grooves prevent the expansion of marks to adjacent tracks. This effect is useful in land/groove recording because it reduces the effect of cross write. The magnetization reversal process depends on the underlayer roughness - as Satoh *et al.*[15] suggested - which is caused by the difference in the pinning effect. A large number of domain wall

pinning sites are required to form uniform mark shapes and to reduce the recording noise.

reference

[1]Y. Mimura and N. Imamura, Appl. Phys. Lett. **28**, 746(1976).

[2]T. Kohashi, H. Matsuyama, C. Haginoya, K. Koike, H. Miyamoto, and J. Ushiyama, Appl. Phys. Lett. **68**, 3350(1996).

[3]K. Kayanuma, T. Iwanaga et al., Proc. SPIE **1316**, 35(1990).

[4]H. W. van Kesteren, A. J. den Boef, W. B. Zeper, J. H. M. Spruit, B. A. J. Jacobs, and P. F. Carcia, J. Appl. Phys., **70**, 2413(1991).

[5]S. Gadetsky, T. Suzuki, J. K. Erwin, and M. Mansuripur, J. Magn. Soc. Jpn., **19**, Suppl., No.S1, 91(1995).

[6]F. J. A. M. Greidanus, W. B. Zeper, B. A. J. Jacobs, J. H. M. Spruit and P. F. Carcia, Jpn. J. Appl. Phys., **28**, 37(1989).

[7]T. Kohashi, H. Matsuyama, C. Haginoya, K. Koike, H. Miyamoto, J. Ushiyama, and H. Awano, J. Mag. Soc. Jpn. **20**, Suppl., No.S1, 303(1996).

[8]J. Ushiyama, H. Awano, H. Miyamoto, K. Ando, T. Kohashi, and M. Takahashi, submitted to Jpn. J. Appl. Phys.

[9]A. Saito, T. Maeda, and H. Sugiyama, Appl. Opt. **27**, 4274(1988)

[10]H. Miyamoto, M. Ojima, T. Toda, T. Niihara, T. Maeda, J. Saito, H. Matsumoto, T. Hosokawa, and H. Akasaka, Jpn. J. Appl. Phys., **32**, 5457(1993).

[11]M. Takahashi, T. Niihara and N. Ohta, J. Appl. Phys.,**64**, 262(1988).

[12]M. Kenny, I. Z. Rahman, M. A. Rahman, B. Bechevet, J. Mouchot and J. Daval, J. Magn. Magn. Mater., **120**, 265(1993).

[13]R. Giles and M. Mansuripur, Comput. Phys., MAR/APR, 204(1991).

[14] M. Mansuripur, R. Giles and G. Patterson, J. Mag. Soc. Japan, **15**,17(1991).

[15]T. Satoh, Y. Takatsuka, H. Yokoyama, S. Tatsukawa, T. Mori, and T. Yorozu, IEEE Trans. Magn. **27**, 5115(1991).

4. Observation of Remanent Magnetization Condition on Obliquely Evaporated Co-CoO Film

4.1 Introduction

Obliquely evaporated metal tape[1-3] has attracted much attention as a high-density magnetic recording medium that has its easy magnetization axis inclined from the surface normal to the film plane. When recording density increases further, the longitudinal recording currently used will suffer serious self-demagnetizing. Perpendicular recording is considered to be suitable for high-density recording because it experiences less self-demagnetizing. But its excellent recording characteristics are supposed to be achieved with a single-pole head, not with the currently used ring head. Obliquely evaporated films have less self-demagnetizing effect than the longitudinally magnetized films and can obtain better recording characteristics than perpendicular magnetized films with the currently used ring head. This makes possible a smooth transition from longitudinally magnetized film to obliquely evaporated film for high-density recording applications. Some obliquely evaporated metal tapes have already been used for high-band 8-mm video tape recorder (VTR) and digital VTR. Especially, a Co-CoO obliquely evaporated film[2,3] has been reported to have the potential to achieve higher recording density because it has high remanent magnetization and coercivity. But for now the recording characteristics

of this medium still do not satisfy the demand for the high-definition VTR film with a track width of about 5 mm, which is half of that in the present digital VTR film.

One of the problems in Co-CoO media was that the origins of the media noise were unclear. Recently we observed the recorded bit structures and magnetization distribution in the remanent state in order to clarify the origins of the media noise and to improve the recording characteristics.[4] We took the images of the bit structures with the in-plane magnetization component using a spin SEM. In the images of Co-CoO,[4] numbers of small inverse domains approximately 80 nm in size were found in recorded bits and remanent magnetization. These domains are considered to be created because of the self-demagnetizing field. In this medium, the origin of most of the media noise is assumed to be inside the bits, because the media noise decreases somewhat as the recording frequency increases.[5] Therefore, these domains are thought to be the principal origin of the media noise.

In this chapter, we study how a high carrier-to-noise (C/N) ratio can be achieved in this medium.[6] It is generally believed that the reduction of the inverse domain sizes is effective in order to reduce the media noise. This is because irregular small flux from the inverse domains are averaged and come close to being constant in a bit if the inverse domains are small enough. To develop a method for reducing the sizes of the inverse domains in this medium, we studied the effect of the field direction on the inverse domain sizes and shapes.

It is difficult to analyze how the field-direction affects the inverse domain under actual recording conditions. This is because the magnetic field from the head diverges

three-dimensionally in space; this causes a change in the strength and the direction on the film according to the position of a point on the film relative to the head. Accordingly, we used several remanent magnetization conditions prepared under an external field with different directions and studied the field-direction effect on the sizes and shapes of the inverse domains.

Besides the media noise reduction, increasing the output signal is also an important issue. When the film's intrinsic anisotropy easy axis is aligned with the component perpendicular to the film plane, the magnetization vectors are likely to incline toward the in-plane direction because of the demagnetization energy,[7] and may form closure-domain-like structures.[8] This results in the decrease of the magnetic flux coming from the media to the head, and consequent decrease of the output signal. This means that analyzing only the in-plane components is not sufficient and that the perpendicular magnetization component should also be considered. Now it is possible by our spin SEM in which all three of the magnetization components are detectable. In this chapter we also discuss the magnetization distributions in three dimensions of this medium.

4.2 Experiment

Co-CoO films were prepared at room temperature by Co deposition on Si-substrates in an oxygen atmosphere at the incident angle of 60 degrees from the substrate surface normal. With this process the magnetization easy axis was directed to

around 30 degrees from the surface normal. The film thickness was about 200 nm. The saturation magnetization of the prepared samples was 950 kA/m, which is higher than the sample in the previous work (700 kA/m).[4] This is because of the reduced oxygen content.

Three kinds of samples of remanent magnetization conditions were prepared by applying the external magnetic field in different directions until the magnetization saturated. Figure 4.1 schematically shows the field directions: (a) the z-direction, (b) the x-direction, and (c) the direction inclined from the z-direction toward the $-x$-direction by 45 degrees.

The condition of the spin SEM measurement is almost the same as in the former chapter. Although this time the samples do not have overcoating layer, sample surface cleaning by Ar^+-ion bombardment is necessary considering the probing depth of this method. In our system, domain images of any two of the three magnetization components can be detected simultaneously.

4.3 Results and Discussion

4.3.2 Magnetization rotation around the domain boundaries

Figures 4.2(a) and 4.2(b) are respectively the spin SEM images of the x- and y-components of remanent magnetization of the same area prepared using the external

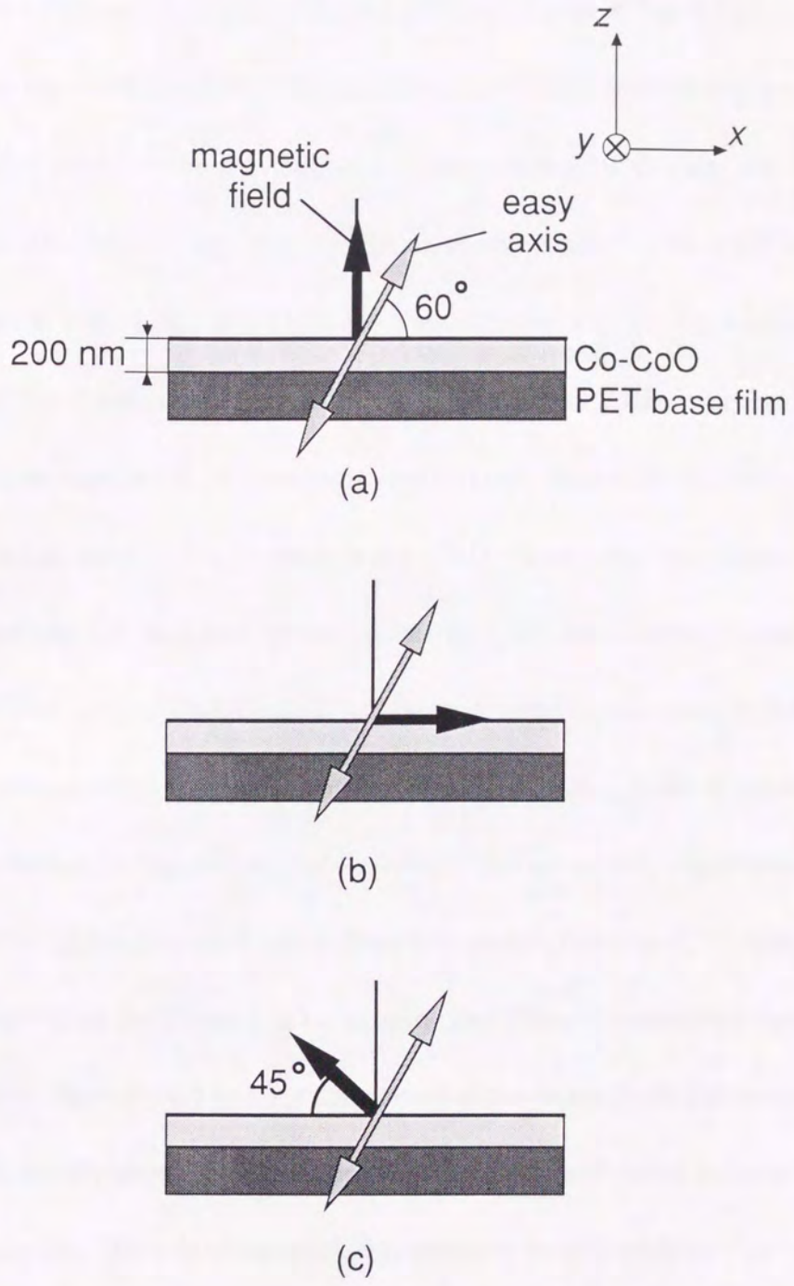

Fig. 4. 1. The structure of the Co-CoO film and the three different directions of the external fields when the remanent magnetization conditions were prepared. :(a) the *z*-direction, (b) the *x*-direction, and (c)the direction inclined from *z*-direction toward - *x*-direction by 45 degrees.[6]

magnetic field perpendicular to the film plane, as shown in Fig. 4.1(a). In Fig. 4.2(a) we can see the small island-like shaped domains, indicated as white regions, similar to the one we observed in the previous work, where these small domains are identified to be the inverse domains by cross sectional domain image.[4] The width of the inverse domains in Figs. 4.2(a) and 4.2(b) are approximately 200 nm. This value is larger than that of the domains we observed in the previous work. This is probably because the medium we used in the present study contains less oxygen and therefore less CoO than the medium used in the previous work. CoO disconnects the magnetic interactions between the Co particles; hence, a smaller CoO ratio means a smaller number of domain walls and inverse domains, and larger inverse domain sizes. In this sense, media noise reduction can be achieved by increasing CoO ratio, however, which also leads to the reduction of the output signal because the saturation magnetization decreases. Therefore increasing CoO ratio does not always increase C/N ratio and there is supposed to be the proper CoO concentration. Since the anisotropy easy axis is in the x-z plane, there should be no y-component of the magnetization if the magnetization is aligned exactly along the easy axis. But the black-and-white contrast in Fig. 4.2(b) indicates that there is substantial y-component in this medium. Figures 4.3 are the domain images of different part of the sample surface from Figs. 4.2. Figures 4.3(a) and 4.3(b) show the images of, respectively the x- and z-components of the same area. These two images show similar domain structures, although the contrast is higher in Fig. 4.3(a) than in Fig. 4.3(b).

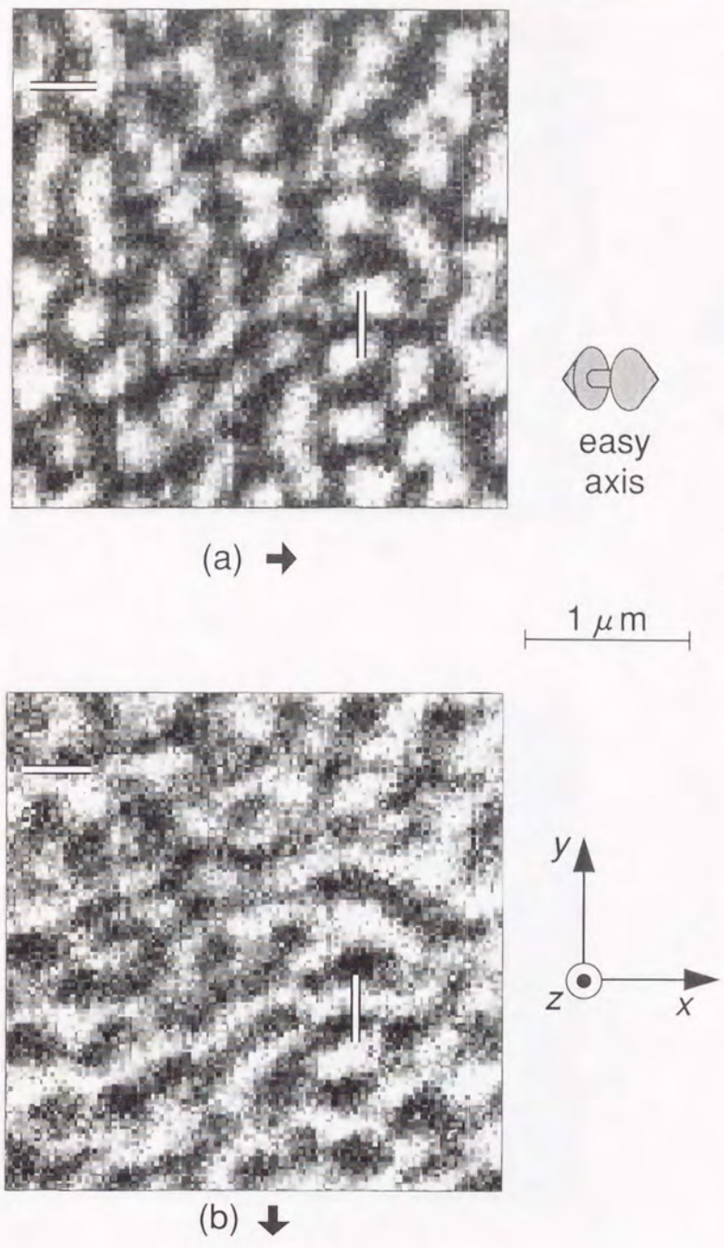

Fig. 4. 2. The spin SEM images of the remanent magnetization conditions of the Co-CoO films. The anisotropy axis is aligned as shown by the gray arrow. The *x*- and *y*-components are shown in (a) and (b), respectively. The arrows below the images indicate the magnetization direction in the images. The black-and-white lines in the images show the region where these two magnetization components are depicted numerically shown in Fig. 4. 4(a) and 4. 4(b), respectively.

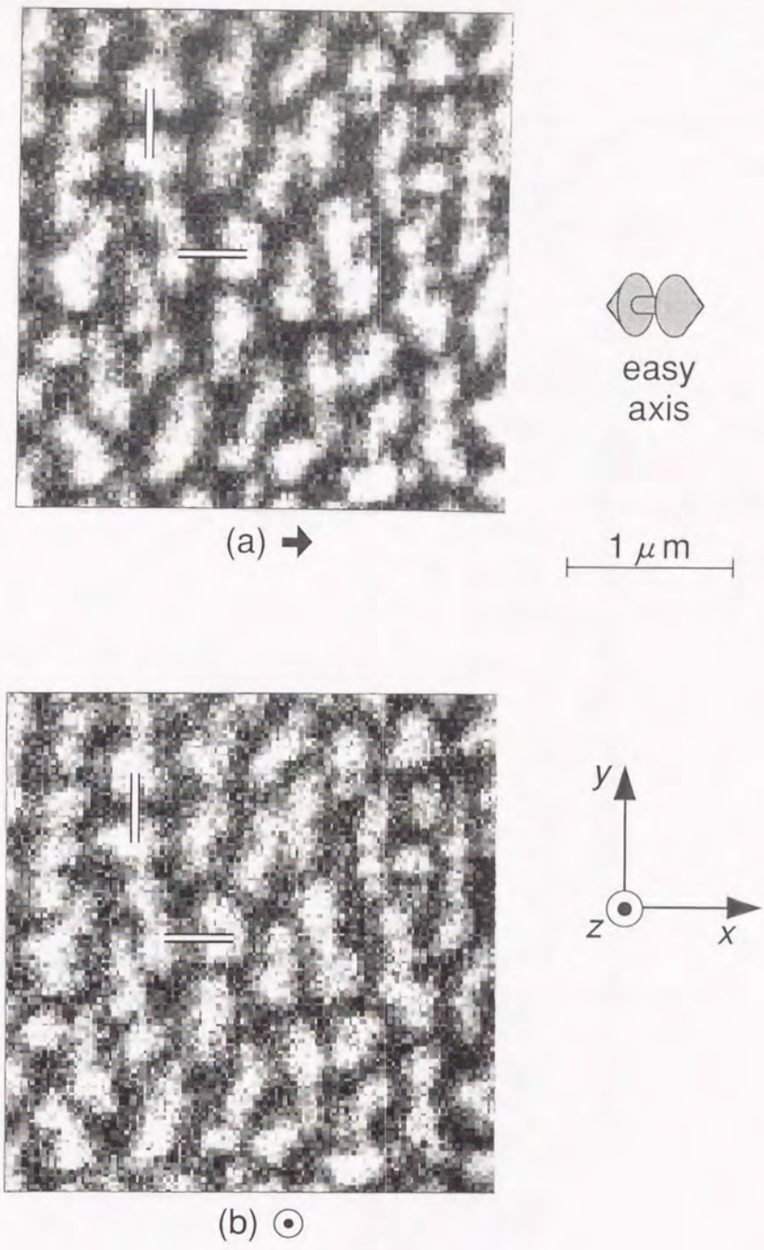

Fig. 4. 3. The spin SEM images of the remanent magnetization conditions of the Co-CoO films. The anisotropy axis is aligned as shown by the gray arrow. The x- and z-components are shown in (a) and (b), respectively. The arrows below the images indicate the magnetization direction in the images. The black-and-white lines in the images show the region where these two magnetization components are depicted numerically shown in Fig. 4. 5(a) and 4. 5(b), respectively.

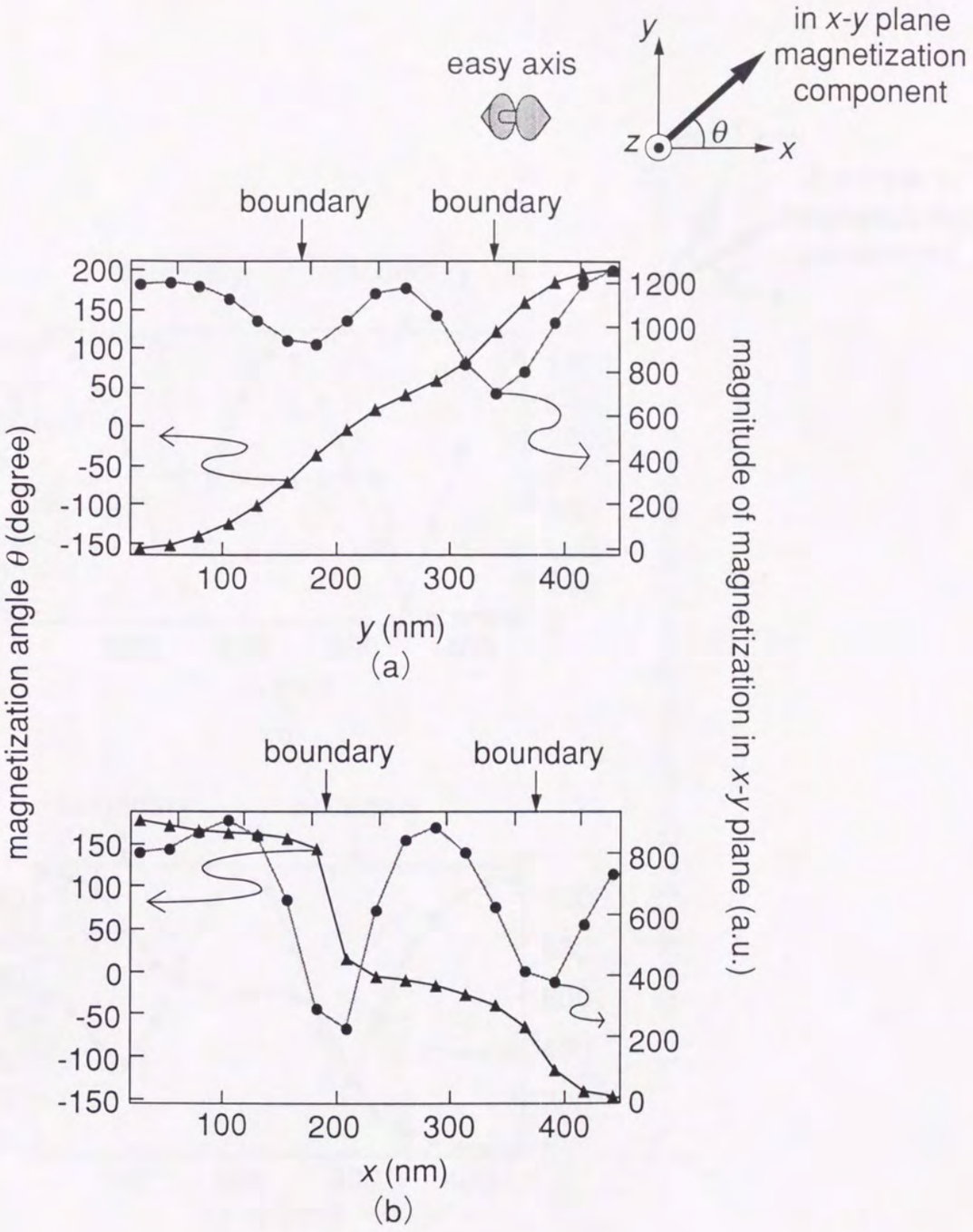

Fig. 4. 4. The angle θ (▲) and the magnitude (●) of the magnetization component in the x-y plane along the black-and-white lines running (a)in the x- and (b)in the y-direction as shown in Figs. 4. 2(a) and 4. 2(b) respectively. The approximate positions of the domain boundaries are indicated above each graph.[6]

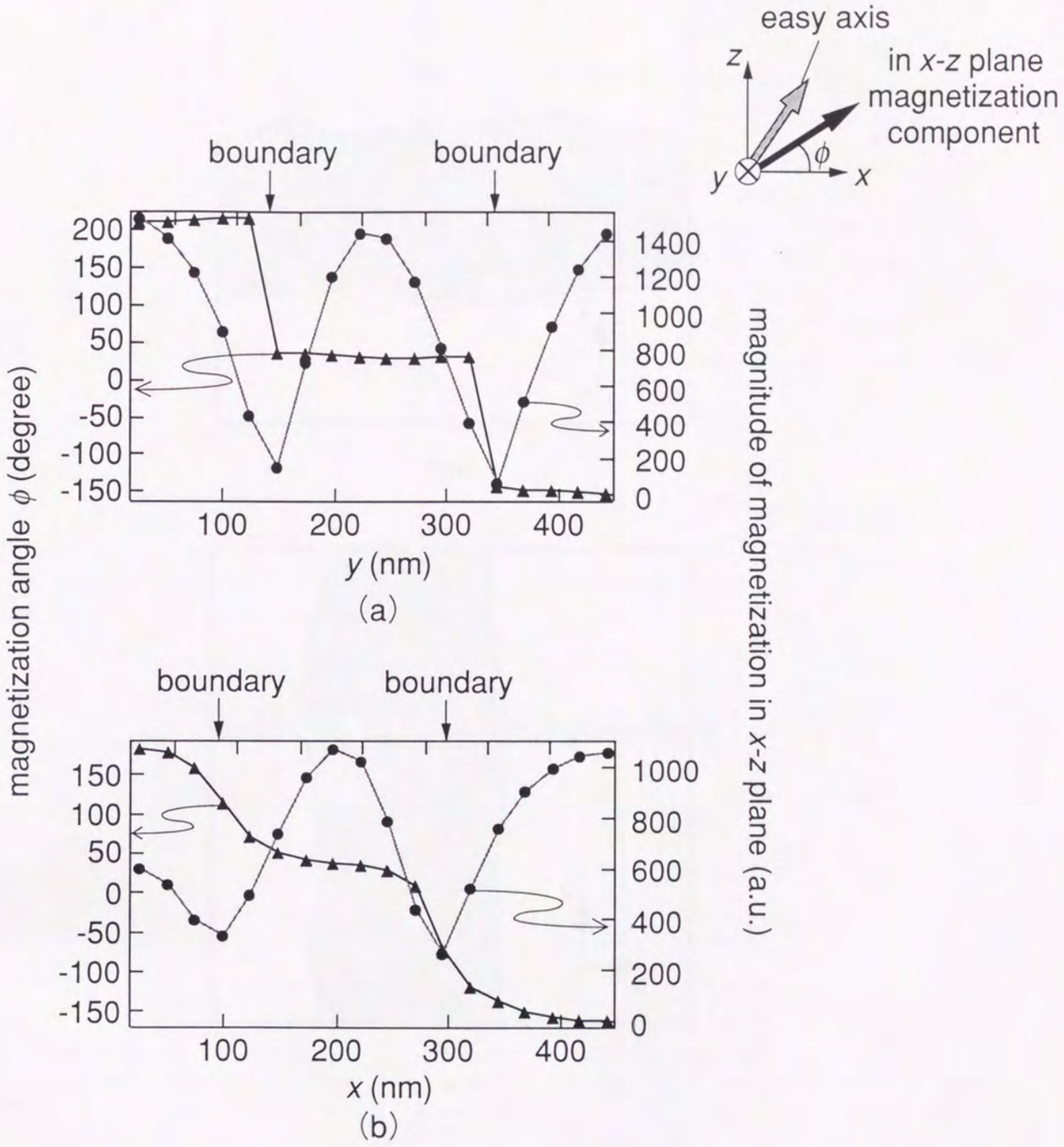

Fig. 4. 5. The angle ϕ (▲) and the magnitude (●) of the magnetization component in the x-z plane along the black-and-white lines running (a)in the x- and (b)in the y-direction as shown in Figs. 4. 3(a) and 4. 3(b) respectively. The approximate positions of the domain boundaries are indicated above each graph.[6]

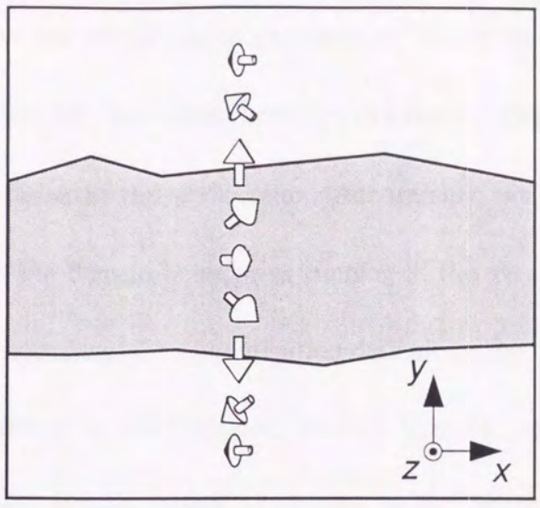

(a)

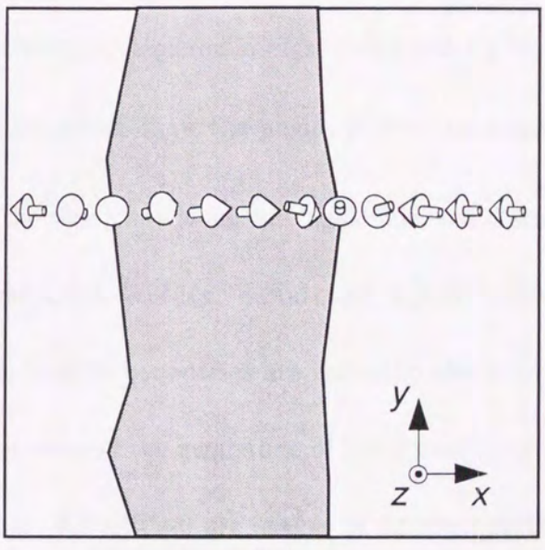

(b)

Fig. 4. 6. The schematic of the magnetization rotation at the surface of the film. Depicted are top view around a domain boundary (a) and (b) along the x-direction. [6]

Each magnetization component was obtained numerically using these domain images. Because the magnetization easy axis inclines in the x–z plane, the way that the magnetization rotates may differ between the domain boundaries running in the x-direction and those in the y-direction. Accordingly, we studied the magnetization rotation across the domain boundaries running in the x- and y-direction. We applied the smoothing operation[9] for magnetization data along the black-and-white lines in the images and analyzed the magnetization rotation in the x–y plane and the x–z plane. See Figs. 4.4(a) and 4.4(b), which show the angle θ and the magnitude of the magnetization component in the x–y plane along the black-and-white lines running in the y- and x- direction, depicted in Figs. 4.2(a) and 4.2(b), respectively. See also Figs. 4.5(a) and 4.5(b), which show the angle ϕ and the magnitude of the magnetization component in the x–z plane along the black-and-white lines running in the y- and x-direction as depicted in Figs. 4.3(a) and 4.3(b), respectively. The approximate positions of the domain boundaries are indicated above each graph; these are defined by the minimum point of the magnitude of the x-component.

Although Figs. 4.2 and 4.3 are images of different parts of the sample surface, the magnetization distribution around the boundaries running in the same directions show similar tendencies. Therefore using Figs. 4.4(a) and 4.5(a), and Fig. 4.4(b) and 4.5(b), the magnetization rotation around a domain boundary running in x- and y-direction can be assumed as shown respectively in Figs. 4.6(a) and 4.6(b), where the black-and-white contrast show the x-component of the magnetization as in Figs. 4.2(a) and 4.3(a). Across the domain boundary running in the x- and y-direction, the

magnetization rotates respectively in the plane including both the easy axis and the y-axis and in the plane inclined slightly from the x-z plane. The validity of this magnetization rotation model can be confirmed if we deduce the angle θ, ϕ and the magnitude of the magnetization from Figs. 4.6, and compare them with those in Figs. 4.4 and 4.5. The magnetization rotation in Fig. 4.6(a) gives a continuous rotation for magnetization components in the x-y plane, but a constant magnetization angle in the domain and a sudden jump at the domain boundary for a magnetization component in the x-z plane. These are explained by the domain images as follows. If we look at the vertical line in Fig. 4.2(a), the magnetization starts out in the $-x$-direction, goes in the $+x$-direction as we move up the line, and ends up in the $-x$-direction. In the case of the same line in Fig. 4.2(b), the magnetization starts out around the boundary of the black and white region, where the y-component is very small. As we move up the line, the magnetization goes in the $-y$-direction, then goes in the $+y$-direction, and ends up around the boundary of the black and white region. As for the case of the vertical line in Figs. 4.3, the polarity of the magnetization change almost in the same way in (a) and (b). These are consistent with the magnetization distribution in Fig. 4.4(a) and 4.5(a). The magnitude of the magnetization component in the x-z plane should be zero at the domain boundary. These values are also consistent with the results in Fig. 4.5(a). Although the magnitude of the magnetization component in the x-y plane should be larger at domain boundary than in domain, the observed result is the opposite as shown in Fig. 4.4(a). This is probably due to the smoothing process or to the probe beam size being larger than the width of the domain boundary.

The magnetization rotation in Fig. 4.6(b) gives the rotation of the magnetization components in both the x-y plane and the x-z plane, which is explained by the domain images in the same way as Fig. 4.6(a). The magnitude of the component in the x-y plane and in the x-z plane should be smallest at the domain boundary. These values are consistent with the results in Figs. 4.4(b) and 4.5(b). However, the decrement of the magnitude in Fig. 4.5(b) is much larger than might be expected from Fig. 4.6(b). This is, again, thought to be due to the smoothing process or to the larger probe beam.

The reasons for these magnetization distributions are considered to be as follows. In obliquely evaporated films, there are magnetic poles in a domain at the surface, which causes the magnetic fluxes to stray above the surface. Because of these stray fields, the magnetization tends to form the closure domains at the film surface to reduce the magneto-static energy.[8] The more gradual magnetization rotation in Fig. 4.4(a) compared to Fig. 4.4(b) suggests that the exchange interaction is stronger in the y-direction than in the x-direction as we suggested in the previous work.[4] This is due to the self-shadowing effect during Co-CoO deposition.[10] In the self-shadowing effect, some of the injected particle beam is prevented from reaching the substrate because of the difference between the injected direction of the particle beam (60-degree-inclination from the surface normal) and the growing direction of the column-shaped particles (30-degree-inclination from the surface normal). This causes the voids between the particles in the x-direction in this case, which results in stronger interparticle exchange interactions in the y-direction than in the x-direction. This

anisotropic exchange interaction is important in considering the field dependency of the remanent domain sizes and shapes, as will be shown later.

The closure-like magnetic domain structure results in the reduction of the magnetic flux coming from the film. If this structure found in under remanent conditions is present in the actual recording, the signals are reduced substantially. Improving the magnetic characteristics of this medium to prevent the formation of this kind of magnetization distribution can be expected to increase the output signal. One method is, for instance, increasing the anisotropy energy of each sample particle, which directs the magnetization in the anisotropy easy axis even at the film surface, in defiance of magneto-static energy.

4.3.3 Field-direction dependency

We studied the field-direction dependency of the inverse domain shapes and sizes. Figures 4.7(a), 4.7(b), and 4.7(c) show the domain structures of the x-component under remanent magnetization conditions with the external field of the directions as shown in Figs. 4.1(a), 4.1(b), and 4.1(c). The sizes and the shapes of the domains clearly change in each figure. As the external magnetic field is applied closer to the anisotropy hard axis, the domain sizes become smaller, especially in the y-direction.

This can be explained qualitatively by considering the relaxation process of magnetization from the saturated state to the remanent state after the external field is removed. When magnetization relaxes from the saturated state in the easy axis

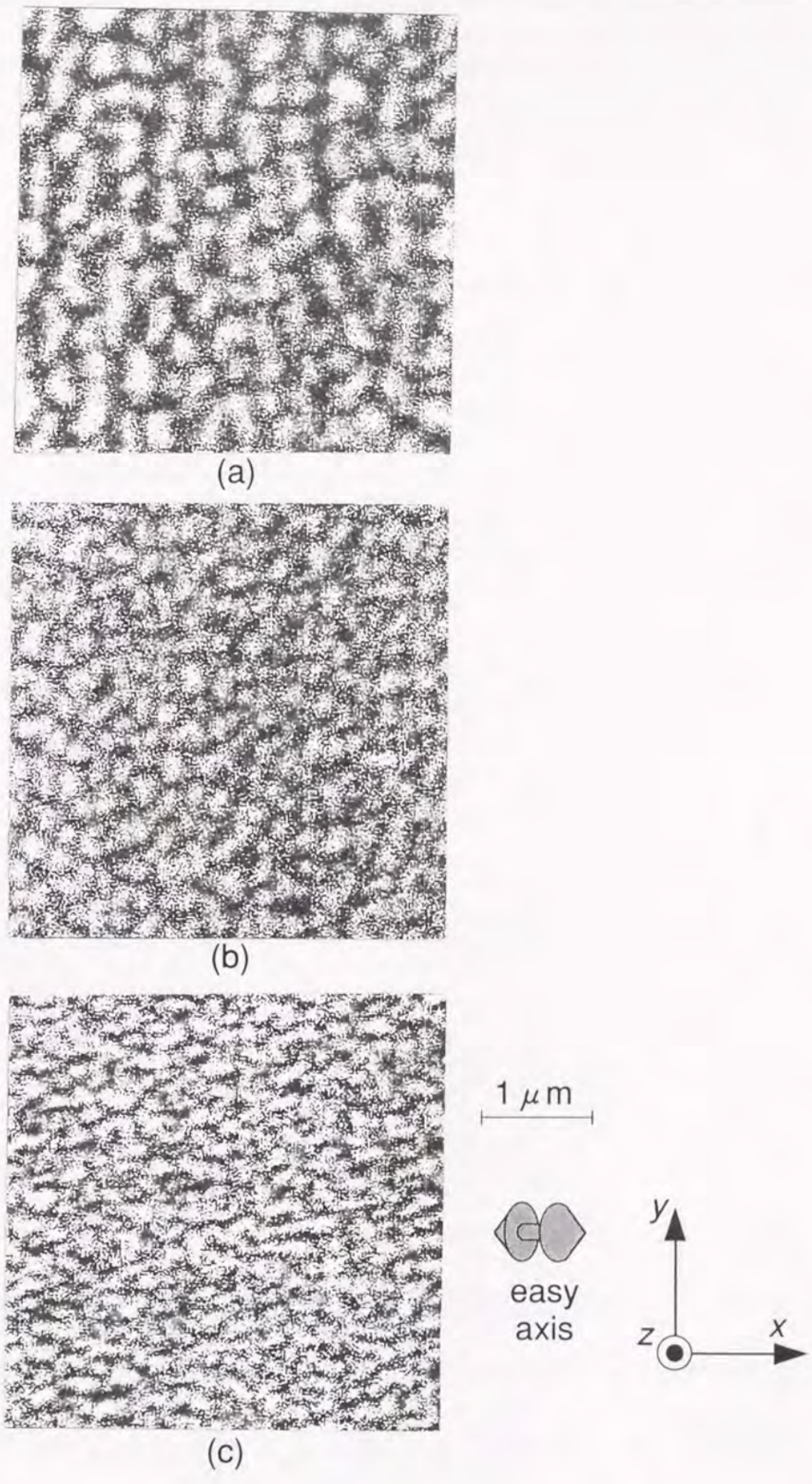

Fig. 4. 7. The remanent magnetization images that were prepared under the three types of external fields. The field directions for (a), (b), and (c) are shown in Figs. 4.1(a), 4.1(b), and 4.1(c), respectively.

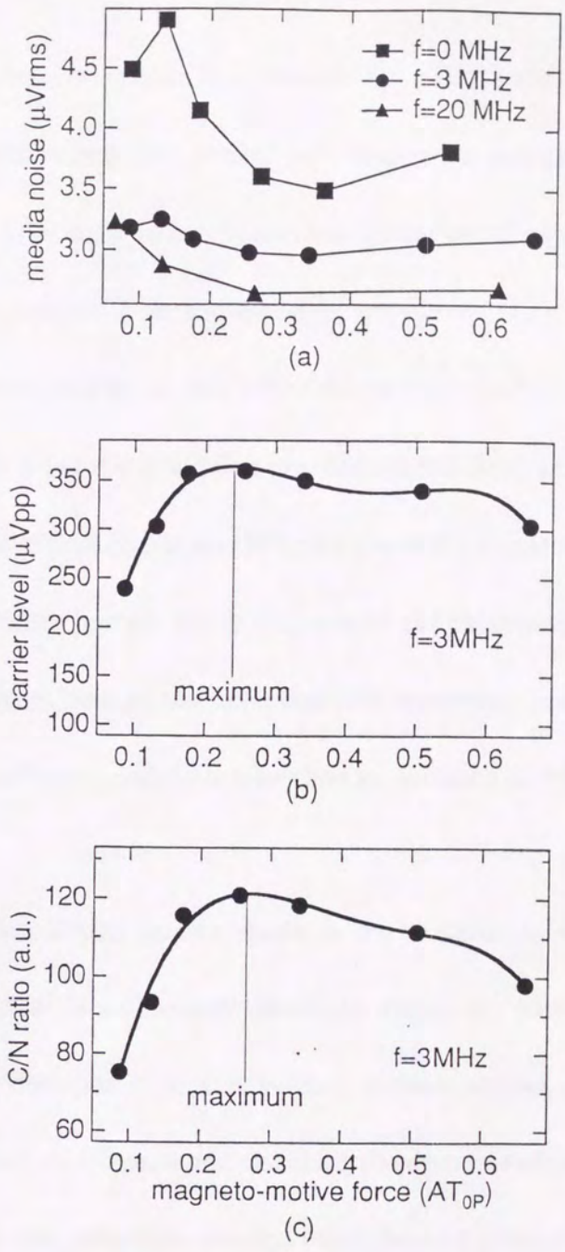

Fig. 4.8. (a) The media noise as a function of the magneto-motive force of the head for the recording frequencies of 0 (dc erase), 3 and 20 MHz. (b) The carrier level and (c) the C/N ratio as functions of the magneto-motive force of the head for the recording frequency of 3 MHz. In (b) and (c), the solid circles are measured data, the line is a fitting curve of fourth degree, and the maximum point of the fitting curve is indicated.[6]

direction, the remanent state is achieved by 180° rotation of parts of the magnetization, overcoming the barrier of anisotropic energy. In this case, the relaxation occurs principally in two steps; the formation of inversion nuclei, and the growth of inverse domains from the nuclei by movement of the domain walls.[11] The second step needs less energy in the case of the medium with the exchange interaction. On the other hand, when the relaxation proceeds in the direction of the hard axis, the remanent state is achieved simply by ±90° rotation of the magnetization without having to overcome an energy barrier. Since the case of the relaxation process in the easy direction needs higher energy (to overcome the anisotropy energy barrier) to form inversion nuclei, its domain density is lower and its domain size is larger, as can be seen in Fig. 4.7(a).

The elongation of the domain shape in the x-direction in Fig. 4.7(c) can be explained by the effect of wall energy. Since the anisotropy easy axis was inclined by 30° toward the x-direction from the medium surface normal, we approximated an inverse domain shape as a square and classified the domain walls into two types in this medium; one lies in the x-z plane, and the other lies in a plane that includes both the y-axis and anisotropy easy axis. If we define these wall areas per unit wall length at the surface respectively as S_x, and S_y,

$$S_x = S_y \cos 30°. \tag{4.1}$$

The respective wall energy of these areas are

$$E_x = 4S_x \sqrt{A_y K} = 4S_y \cos 30° \sqrt{A_y K} \tag{4.2}$$

and

$$E_y = 4S_y \sqrt{A_x K} . \qquad (4.3)$$

Here A_x and A_y are the interparticle exchange constant in x- and y-direction respectively, and $A_x < A_y$ is as we mentioned before. K is the anisotropy constant and has no direction dependency. If $\cos 30° \sqrt{A_y} < \sqrt{A_x}$, $E_x < E_y$, and the wall tends to run in the x-direction to save wall energy and the domain stretches in the x-direction.

The domain shapes in Fig. 4.7(a) can be explained as follows. During the process of the inverse domain growth from the inversion nuclei, the domain wall tends to move more easily in the y-direction than in the x-direction, since the exchange energy A_y is larger in the y-direction[11,12]. This phenomenon tends to make the domain longer in the y-direction. But the domain shape is disadvantageous in view of the effect of wall energy as discussed above. Thus the real domain shape is determined by the balance of the mobility and the energy of the wall, and is almost circular or a little elongated in the y-direction.

We can take advantage of this result to reduce media noise. Besides the remanent magnetization conditions, there are many small inverse domains in the recorded bits that are considered to be the principal source of media noise.[4] In the process of recording, the media magnetization changes direction due to the fields from the head. The fields from the head are distributed three-dimensionally; consequently, the strength and the direction change from point to point on the film according to the relative position of the head and the medium. The field is directed close to the easy axis at the leading side and close to the hard axis at the trailing side in the case of the obliquely evaporated medium. The position of the field, that last affects the film

magnetization, moves to the trailing side when the magneto-motive force increases. When the alignment of that field is close to that of the hard axis (i.e., that means when the magnetization is released in the remanent condition from the saturation in the hard axis direction) the inverse domain sizes can be expected to become small. This condition will lead to reduction of media noise. Therefore we assumed that this is the best magneto-motive force from the standpoint of the media noise reduction.

We studied the relation between the magneto-motive force of the head and media noise. We recorded on the film using the ring head at three recording frequencies, 0 (dc erase condition), 3, and 20 MHz, and measured the media noise as a function of the magneto-motive force. The results are shown in Fig. 4.8(a). The media noise decreases as the recording frequencies increase. This tendency agrees with the noise characteristics formerly reported.[5] At every frequency, as the magneto-motive force increases from zero, the media noise decreases; it reaches minimum around 0.3 ampere-turn-zero-to-peak (AT_{0P}). Increasing the magneto-motive force further from this level increases the media noise. This phenomenon of the minimum point of the media noise as a function of the magneto-motive force has been reported previously,[13] although the direction of the magnetization easy axis in the medium was different from our case (it was inclined by 60 degrees from the surface normal in the case of Ref. 12). We assume that the field from the head, which runs in the hard axis direction, becomes the last field to affect the film magnetization and that the inverse domain sizes are minimal around the magneto-motive force of 0.3 AT_{0P}.

To consider the C/N ratio, we need to study not only noise but also carrier level. When the external field is applied in the anisotropy hard axis, the remanent magnetization decreases. In this sense, the carrier level is also assumed to decrease at the magneto-motive force that decreases the media noise. But the carrier level is also affected by the spatial gradient of the field from the head around the coercive force, which affects the magnetization distribution at the bit boundaries. Figure 4.8(b) shows the carrier level as a function of the magneto-motive force at the recording frequency of 3 MHz. The solid circles are measured data, the solid line is a fitting curve of the fourth-degree-polynomial, and the maximum point of the fitting curve is indicated. From 0 AT_{0P}, the carrier level increases drastically with the magneto-motive force and reaches the maximum around at 0.25 AT_{0P}. After that it decreases gradually. The carrier level is not small around the magneto-motive force where the media noise reaches the minimum. That means that the carrier level depends mainly on the field gradient around the coercive force, while the media noise is determined mainly by the field direction that last affects the magnetization field. Therefore, the characteristics of the carrier level, and of the media noise as a function of the magneto-motive force of the head, are not the same. Figure 4.8(c) shows the C/N ratio as a function of the magneto-motive force of the head, which is calculated from Fig. 4.8(a) and 4.8(b). Again, the solid circles are the measured data, the solid line is a fitting curve of the fourth-degree-polynomial, and the maximum point of the fitting curve is indicated. It reaches the maximum between the magneto-motive force where the carrier level reaches the maximum, and the magneto-motive force where the media noise reaches

the minimum. This indicates that the field direction from the head and resulting domain sizes play important roles in increasing the C/N ratio in obliquely evaporated recording media.

4.4 Conclusion

The remanent magnetization conditions of obliquely evaporated recording media Co-CoO films were studied. We found that the surface with a lot of inverse domains has a closure-domain-like structure, and the inverse domain size is smaller when the field is applied in the hard-axis direction. Application of these results to recording affords the capability of increasing the output signal by increasing the anisotropy energy to prevent the formation of closure-like domain structure, and of decreasing the media noise when the last field from the recording head, which determines the magnetization condition of the media, is aligned in the direction of the hard axis.

references

[1]A.Tomago, J.Inst.TV.Eng.Jpn. **35**, 733(1981) (in Japanese).

[2]T.Kawana, S.Onodera and T.Samato, IEEE Trans.Mag. **31**, 2865(1995).

[3]K.Yoshida and T.Takayama, J.Mag.Mag.Matter. **82**, 228(1989).

[4]H.Matsuyama, T.Kohashi, K.Koike, and T.Takayama, J.Magn.Soc.Jpn. **20**, 795(1996).

[5]M.Futamoto and Y.Honda, J. Magn. Soc. Jpn. **18**, Suppl. S1, 485(1994).

[6]T.Kohashi, H.Matsuyama, K.Koike, and T.Takayama, J. Appl. Phys. **81**, 7915(1997).

[7]J.Unguris, M.R.Scheinfein, R.J.Celotta, and D.T.Pierce, Appl.Phys.Lett. **55**, 2553(1989).

[8]S.Iwasaki and Y.Nakamura, IEEE Trans.Mag.**13**, 1272(1977).

[9]P.Marchand and L.Marmet, Rev.Sci.Instrum. **54**, 1034(1983). In this paper we calculated as follows:

$Y_i = ((X_{i-5}+X_{i+5}) + 10\ (X_{i-4}+X_{i+4}) + 45\ (X_{i-3}+X_{i+3}) + 120\ (X_{i-2}+X_{i+2}) + 210\ (X_{i-1}+X_{i+1}) + 252X_i)/1024$.

Here, X_i and Y_i are the measured and smoothed data at the ith data point.

[10]J.A.Thornton, J.Vac.Sci.Technol., **11**, 666(1974).

[11]J.Zhu and H.N.Bertram, J.Appl.Phys., **66**, 1291(1989).

[12]U.F.Gianola, D.H.Smith, A.A.Thiele and L.G.Van Uitert, IEEE Trans.Mag. **MAG-5**, 558(1969).

[13]T.Ishida, R.Sugita and K.Thoma, J. Magn. Soc. Jpn. **19**, 173(1995).

5. Summary

In this study we have improved our spin SEM, which was developed by Matsuyama *et al.* for detecting perpendicular magnetization component, which was not able to be detected, by installing the spin rotator. By the spin SEM we observed the recorded marks on magneto-optical recording medium TbFeCo and remanent magnetization state of obliquely evaporated Co-CoO film. We summarized the main conclusions of the present work as follows.

[1] A spin rotator for detecting the magnetization component perpendicular to the sample surface by spin SEM was developed. The spin rotator needs a large focusing area for this purpose and the computer simulation showed that a conventional spin rotator, which is a well-known energy filter named a Wien Filter, can be modified to have a large focusing area by using hyperbolic cylindrical pole pieces as a magnet and several auxiliary electrodes and satisfy our demand. We confirmed all the secondary electrons emitted from the area of a surface as large as 1 mm in diameter can pass the spin rotator with uniform spin rotation, and the distribution of the perpendicular magnetization components can be imaged successfully by spin SEM.

[2] The recorded marks of magneto-optical media TbFeCo were observed. From the laser power dependency of the mark shapes and sizes on the land/groove substrate we confirmed that the borders between lands and grooves prevent the expansion of marks to adjacent tracks. This effect is useful in land/groove recording where the track pitch becomes smaller substantially, because it reduces the effect of cross write. Moreover we confirmed that the underlayer roughness affects the magnetization reversal process.

This is considered to be due to the difference in the pinning effect. For the purpose of the media noise reduction, a large number of domain wall pinning sites are required to form uniform mark shapes.

[3] The remanent magnetization conditions of obliquely evaporated recording media Co-CoO films were studied. We found that the surface with a lot of inverse domains has a closure-domain-like structure, which causes the reduction of the output signal of this medium. Increasing the output signal will be achieved by increasing the anisotropy energy to prevent the formation of closure-like domain structure. The inverse domain size is smaller as the field is applied in the magnetization hard-axis direction when the remanent condition is prepared. This result suggests the media noise decreases when the last field from the recording head, which determines the magnetization condition of the media, is aligned in the direction of the magnetization hard axis.

Acknowledgment

The author expresses his most sincere gratitude to Prof. Yoshihito Miyako of Osaka University for critical reading of this manuscript and stimulating discussions.

This work reported here was carried out at Advanced Research Laboratory (ARL), Hitachi, Ltd. The author gives thanks to Drs. Shojiro Asai, former general-manager, Katsumi Miyauchi, present general-manager, Atsushi Suzuki, former vice-manager of ARL, Hitachi, Ltd. for giving him opportunity to conduct this research. He also thanks to Dr. Kazuyuki Koike (ARL, Hitachi, Ltd.) for his continuous stimulus and invaluable discussions on various aspects throughout the course of this work. He is very thankful to Dr. Hideo Matsuyama (ARL, Hitachi, Ltd.) for his kind advise about operating the spin SEM and designing the spin rotator, and precious discussions on various aspects throughout the course of this work. The author would like to thank Dr. Youichi Ose of Hitachi Research Laboratory, Hitachi, Ltd. and Mr. Toshio Okochi of Central Research Laboratory, Hitachi, Ltd. for their kind advise about the computer simulations for designing the spin rotator. He is also thankful to Dr. Katsushige Tsuno of JEOL, Ltd. for helpful discussion about designing the spin rotator. He also thanks Mr. Yoshimasa Kondo of Instrument Division, Hitachi, Ltd., Mr. Masahiko Hamasaki of Central Research Laboratory, Hitachi, Ltd., Mr. Shigeo Kubota, Mr. Shoukichi Matsunami, and Mr. Noboru Moriya of ARL, Hitachi, Ltd. for their technical support in designing and constructing the spin rotator. He also thanks Dr. Harukazu Miyamoto, Mrs. Junko Ushiyama of Central Research Laboratory, Hitachi, Ltd. and Dr. Hiroyuki Awano of Recording Media Research Laboratory of Hitachi Maxell, Ltd. for the sample

preparation of GdFeCo and TbFeCo and invaluable discussions. He also thanks Mr. Takanobu Takayama of Recording Media Research Laboratory of Hitachi Maxell, Ltd. for the sample preparation of Co-CoO and fruitful discussions. He would like to thank Dr. Uesaka of Central Research Lab., Hitachi, Ltd., for his valuable discussion about analyzing the domain images of Co-CoO. His thanks are also extended to his colleagues, Mr. Takashi Furukawa and Mr. Chiseki Haginoya, in his group who helped directly and indirectly with his research.

Finally, the author wishes to especially thank Mrs. Emi Kohashi of ARL Hitachi,Ltd. for her support during the long term study of this work.

List of publications

1. K. Kindo, M. Honda, T. Kohashi, and M . Date, J. Phys. Soc. Jpn. **59**, No.7, 2332(1990). "Electron spin resonance in cupric oxide"

2. T. Kohashi, M. Ono, M. Date, A. Yamagishi, X. P. Zhong, Q. Wang, F. M. Yang, R. J. Radwanski, and F. R. de Boer, J. Appl. Phys. **69**, No.8, 5542(1991). "Field-induced non-collinearity of the magnetic moments in $Gd_2Co_{14}B$"

3. T. Kohashi, F. R. de Boer, R. J. Radwanski, X. P. Zhong, A. Yamagishi, M. Date, J. Phys. Soc. Jpn. **60**, No.10, 3543(1991). "High field magnetization of $Er_2(Fe, Al)_{14}B$"

4. T. Kohashi, K. Kindo, F. R. de Boer, R. J. Radwanski, X. P. Zhong, A. Yamagishi, M. Date, Physica B **177**, 215(1992). "High field magnetization process in $Er_2(Fe, Al)_{14}B$"

5. R. J. Radwanski, F. R. de Boer, X. P. Zhong, F. M. Yang, Y. J. Li, T. Kohashi, M. Ono, M. Date, A. Yamagishi, J. Mag. Mag. Mater. 101, 392(1991). "Field induced noncollimear magnetic-structures in $Er_2Fe_{14}B$-based compounds"

6. R. J. Radwanski, X. P. Zhong, F. R. de Boer, F. M. Yang, Y. J. Li, T. Kohashi, M. Ono, M. Date, A. Yamagishi, J. Mag. Mag. Mater. 104, 1139(1992). "Field induced noncollimear magnetic-structures in $Er_2Fe_{14}B$-based compounds"

7. T. Kohashi, H. Matsuyama, K. Koike, and H. Miyamoto, J. Mag. Soc. Jpn. **18**, Suppl., No.S1, 7(1994). "A spin rotator used for detecting all three magnetization vector components in spin-polarized scanning electron microscopy"

8. T. Kohashi, H. Matsuyama, and K. Koike, Rev.Sci.Instrum. 66,5537(1995). "A spin rotator for detecting all three magnetization vector components by spin-polarized scanning electron microscopy"

9. T. Kohashi, H. Matsuyama, C. Haginoya, K. Koike, H. Miyamoto, and J. Ushiyama, Appl. Phys. Lett. 68, 3350(1996). "Mark observation of TbFeCo recorded on land/groove substrate by spin-polarized scanning electron microscopy"

10. T. Kohashi, H. Matsuyama, C. Haginoya, K. Koike, H. Miyamoto, J. Ushiyama, and H. Awano, J. Mag. Soc. Jpn. 20, Suppl., No.S1, 303(1996). "Recorded mark observation by spin-polarized scanning electron microscopy"

11. J. Ushiyama, H. Awano, H. Miyamoto, K. Andoh, T. Kohashi, and M. Takahashi, submitted to Jpn. J. Appl. Phys. "Effect of underlayer surface roughness upon the magnetic properties and noise characteristics of magneto-optical disks"

12. H.Matsuyama, T.Kohashi, K.Koike, and T.Takayama, J.Magn.Soc.Jpn. 20, 795(1996). "Direct observation of high-density recorded bits in Co-CoO obliquely evaporated media with a spin-polarized scanning electron microscope"

13. T.Kohashi, H.Matsuyama, K.Koike, and T.Takayama, to be published in J. Appl. Phys., "Observation of remanent magnetization condition on obliquely evaporated Co-CoO film".

14. Y. Tanaka, N. Suzuki, T. Kohashi, and S. Yonezawa, submitted to Jpn. J. Appl. Phys. "Laser-pumped magnetic field modulation optical recording"